Control of MgSO40(aq) on the transformation of amorphous calcium carbonate to high-Mg calcite and long-term reactivity of the crystalline solid

Katja E Goetschl, Martin Dietzel, Bettina Purgstaller, Cyrill Grengg, Vasileios Mavromatis

Available online at www.sciencedirect.com

ScienceDirect

Geochimica et Cosmochimica Acta 312 (2021) 357–374

Geochimica et Cosmochimica Acta

www.elsevier.com/locate/gca

Control of $MgSO_4^0(aq)$ on the transformation of amorphous calcium carbonate to high-Mg calcite and long-term reactivity of the crystalline solid

Katja E. Goetschl [a,*], Martin Dietzel [a], Bettina Purgstaller [a], Cyrill Grengg [a], Βασίλειος Μαυρομάτης (Vasileios Mavromatis) [b]

[a] Institute of Applied Geosciences, Graz University of Technology, Rechbauerstrasse 12, 8010 Graz, Austria
[b] Géosciences Environnement Toulouse (GET), CNRS, UMR 5563, Observatoire Midi-Pyrénées, 14 Av. E. Belin, 31400 Toulouse, France

Received 15 April 2021; accepted in revised form 21 July 2021; available online 11 August 2021

Abstract

The Mg and SO_4 content of naturally occurring calcite are routinely used as paleoenvironmental proxies. Yet little is known about the mechanisms governing the presence of these ions in carbonate minerals when their formation proceeds via an amorphous precursor. To address this, the transformation of Mg-free amorphous calcium carbonate (ACC) into nanocrystalline high-Mg calcite (HMC) was experimentally studied in solutions containing 27 mM of Mg and a range of 10–90 mM of SO_4. The obtained results suggest that ACC is stable for several minutes in the experimental solutions and this amorphous phase actively uptakes Mg and SO_4 that are incorporated in its structure. Additionally, the obtained results suggest that the stabilization of ACC is not affected by its Mg content and that the transformation to HMC is effectively controlled by the abundance of the free $Mg^{2+}(aq)$ ion. The transformation of ACC to HMC occurs earlier at elevated SO_4 concentrations because SO_4 limits the availability of $Mg^{2+}(aq)$ due to the formation of the $MgSO_4^0(aq)$ complex. The HMC that is formed from ACC appears as aggregates composed of nanocrystallites and exhibits Mg and SO_4 contents up to 8 and 2 mol% depending on the initial SO_4 concentration in the reactive solution. The precipitated HMC was kept in contact with the reactive solution in order to assess its reactivity for up to 1 year of reaction time. Over time, a continuous exchange of Mg and SO_4 between calcite and reactive solution was observed resulting in enrichment of Mg and depletion of SO_4 affecting the total mass of the aggregates with the distribution of these elements to appear homogeneous in the crystalline solid. The high reactivity and the continuous exchange of solutes between the nanocrystalline calcite and the reactive solutions limits the use of Mg and SO_4 content of these HMCs as environmental proxies.

Keywords: amorphous calcium carbonate; aqueous complexation; high-Mg calcite; nanocrystalline; reactivity; Mg and SO_4 incorporation

1. INTRODUCTION

Calcium carbonate ($CaCO_3$) formation in aqueous environments results in minerals containing traces or foreign elements (Morse and Mackenzie, 1990; Reeder, 1990; Dietzel 2011). The chemical and isotopic composition of $CaCO_3$ are routinely used in order to reveal the environmental conditions that occurred at the time of mineral formation. Nowadays it is well accepted that the chemical/isotopic signals recorded in carbonates are affected by a number of parameters including temperature (e.g. Burton and Walter, 1991), pH (e.g. Mavromatis et al., 2015; Uchikawa et al., 2017), growth kinetics (e.g. Lorens, 1981) aqueous

* Corresponding author.
E-mail address: katja.goetschl@tugraz.at (K.E. Goetschl).

https://doi.org/10.1016/j.gca.2021.07.026
0016-7037/

complexation (e.g. Mavromatis et al., 2017a) and mineralogy (e.g. Mavromatis et al., 2018). However, less is known about the mechanisms governing the chemical/isotopic composition of carbonate minerals when the formation proceeds via an amorphous precursor (Evans et al., 2020). Amorphous calcium carbonate (ACC) has been identified as precursor phase for crystalline $CaCO_3$ in many calcifying biomineralization strategies (Du and Amstad, 2020; and references therein). Owing to the importance of ACC in biomineralization it has been the subject of research for a large number of studies in the last two decades (e.g. Raz et al., 2000; Addadi et al., 2003; Gower, 2008; Long et al., 2011; Gong et al., 2012; Albéric et al., 2018; Jin et al., 2018). Novel non-classical nucleation concepts of amorphous intermediates have been proposed and numerous studies exist that show a wide variety in the hydration level of ACC and the characteristics of its short-range order (Gebauer et al., 2010; Gebauer and Cölfen, 2011; Schmidt et al., 2014; De Yoreo et al., 2015; Sun et al., 2016; Tobler et al., 2016; Du et al., 2018; Mergelsberg et al., 2020).

A large number of experimental studies has explored the mechanisms controlling the transformation of ACC into crystalline $CaCO_3$ polymorphs (e.g. Rodriguez-Blanco et al., 2012; Rodriguez-Navarro et al., 2015; Giuffre et al., 2015; Blue et al., 2017; Purgstaller et al., 2017a,b; Zou et al. 2018). It is for example well known that high-Mg calcite (HMC) with Mg contents exceeding 4 mol% is often formed via the formation and transformation of Mg-bearing ACC by mixing a carbonate-bearing solution with a Ca-Mg-rich solution (e.g. Mavromatis et al., 2012; Long et al., 2014; Purgstaller et al., 2016; Xto et al., 2019). Moreover, the presence of Mg has been shown to temporary stabilize ACC and to retard its transformation in solution (e.g. Loste et al., 2003; Politi et al., 2010; Lin et al., 2015; Konrad et al, 2018). Although the role of Mg in stabilizing ACC has been well studied, significant gaps of knowledge exist with respect to the effect of other ions on the ACC transformation pathway. For example, although SO_4 is the second most concentrated anion in seawater, only a few studies have examined the effect of SO_4 on the stability and reactivity of the amorphous precursor (Bots et al., 2012; Ihli et al., 2013; Han et al., 2017).

In the presence of aqueous Mg, the transformation of ACC results mostly in the formation of nanocrystalline calcite agglomerations (e.g. Jiang et al., 2011; Long et al., 2011; Blue et al., 2017; Huang et al., 2018; Xto et al., 2019). In this context, an aspect of great importance is the reactivity of the nanocrystalline calcite when in contact with an aqueous solution. The amorphous solid is only present at the initial stages of mineral formation, whereas the nanocrystalline calcite remains in contact with the solution for extended periods of time. In the latter case, the large surface area of the nanocrystalline calcite aggregates can be subject to continuous exchange of solutes (Mavromatis et al., 2017b; Oelkers et al., 2019). Detailed understanding of the distribution of trace elements and isotopes after the transformation of ACC is still largely lacking, but essentially required in order to support geochemical proxies and to unravel information of their (past) formation conditions that is archived in abiotic and biogenic calcite.

The present study explores two features related to calcite formation via ACC: the first is assessing the role of SO_4 in the transformation process and the second is the long-term reactivity of the crystalline product formed from ACC. Thus, ACC transformation experiments were conducted in the presence of aqueous Mg^{2+} and SO_4^{2-} ions and the crystalline solids were kept in contact with the reactive solution for 1 year of reaction time. The experimental set-up allowed to distinguish between (i) the elemental distribution between ACC and reactive solution and (ii) the redistribution during its transformation to calcite. The molar Mg/SO_4(aq) ratios were varied in order to systematically study the coupled effect of Mg and SO_4 on (i) the elemental exchange between solid ACC and the aqueous phase as well as the stability of ACC, (ii) the transformation kinetics of ACC and (iii) the Mg content of calcite formed via an amorphous precursor. Reactivities of ACC and HMC, elemental distribution and nanostructured features of solid phases are discussed in the scope of (i) their importance for the interpretation of individual proxy data derived from amorphous-to-crystalline carbonate archives and (ii) the limits of Mg and SO_4 distribution in nanocrystalline HMC to reconstruct bulk precipitating water.

2. METHODS

2.1. Synthesis of ACC

Synthetic ACC was prepared following the protocol described earlier in Konrad et al. (2016). Briefly, 80 mL of a 250 mM $CaCl_2$ solution were poured into a glass beaker containing the same volume of a 250 mM Na_2CO_3 solution and mixed vigorously for 2–3 s. The solid product of the reaction was separated immediately from the solution by a 0.2 μm cellulose membrane filter using suction filtration. Subsequently, the solid phase was rinsed with ultrapure deionized water to remove Na^+ and Cl^- ions and immediately freeze-dried using a Virtis Benchtop 3L freeze-dryer in order to remove adsorbed water. The synthesis protocol was repeated several times in order to prepare a batch of about 18 g of synthetic ACC as starting material for the transformation experiments. The freeze-dried ACC was stored in a closed vial in a desiccator with silica gel (relative humidity = 3%) to prevent its transformation to crystalline $CaCO_3$.

2.2. Experimental set-up

The transformation of synthetic ACC to calcite was performed in a glass reactor, equipped with a Teflon® coated magnetic stirrer operating at 350 rpm. The reactor initially contained 50 mL of a Mg (and SO_4) -bearing solution (Fig. 1). The experiments were performed at 23 ±1 °C and at pH 8.3 ±0.2 that was adjusted automatically through the titration of a 0.5 M NaOH solution (titrator TitroLine® 7800 from SI Analytics). The initial reactive solution contained ~100 mM $NaHCO_3$ and ~27 mM $MgCl_2$ at pH ~ 8. The SO_4^{2-} concentrations in the initial solutions ranged between 10 and 90 mM (see Table 1). The experiments were labeled as sX, where X refers to the respective

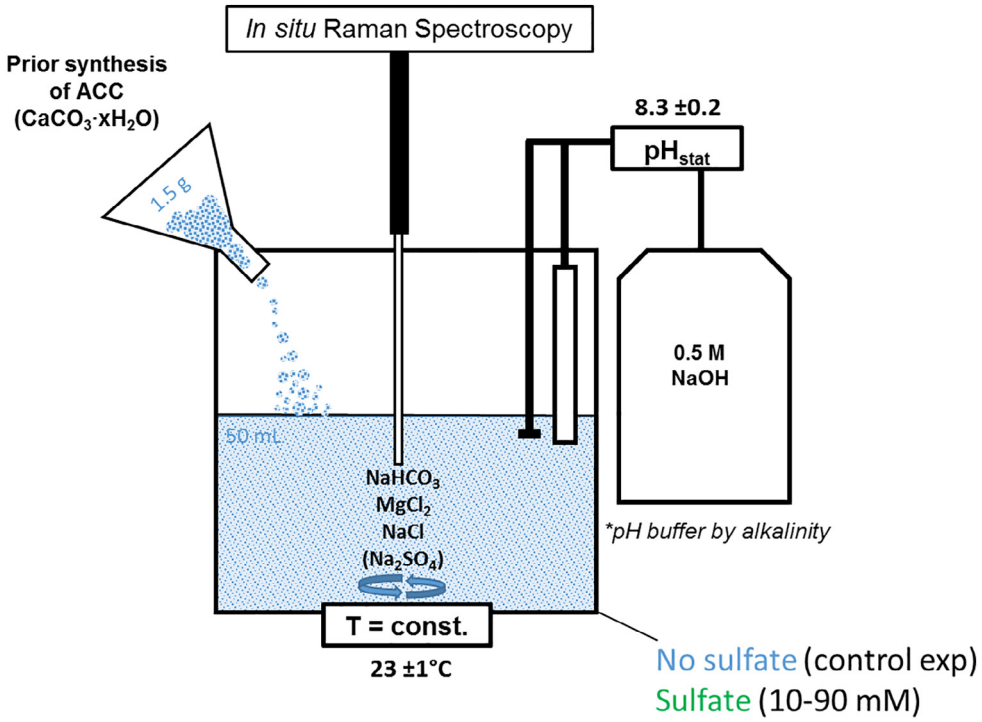

Fig. 1. Experimental set-up of ACC transformation experiments. Synthetic ACC was added to the reactor containing a HCO_3-Mg-(SO_4-) bearing solution. The mineral transformation reaction occurred under controlled physicochemical conditions and was monitored *in situ* by Raman spectroscopy.

concentration of SO_4 (mM) in the initial reactive solution. The experiment with SO_4 concentration of 30 mM was performed in duplicate and was labeled s30_2. A control experiment was conducted in the absence of SO_4 and was labeled s0. The background electrolyte concentration of the initial reactive solutions was adjusted to 330 mM by the addition of NaCl when necessary. All solutions were prepared using ultrapure deionized water and analytical grade chemicals from Roth ($CaCl_2 \cdot 2H_2O$, $MgCl_2 \cdot 6H_2O$, $NaHCO_3$, Na_2CO_3, Na_2SO_4, NaCl).

At the beginning of the experiment 1.5 g of ACC was introduced into the reactive solution following a similar approach to Konrad et al. (2018) and Purgstaller et al. (2019). The immersion probe of an *in situ* Raman spectrometer was placed into the suspension to monitor the temporal evolution of the solid phase transformation and the vibrational spectra of dissolved species for about 1 h of reaction time. In order to characterize both, the chemical composition of the solution and the solid phase, homogeneous subsamples (1.5 mL) were collected under stirring with a pipette at certain reaction times (Table 1). The solid material was immediately separated from the reactive solution with the aid of a 0.2 µm cellulose acetate membrane filter using suction filtration, subsequently rinsed extensively with ethanol and dried in the oven at 40 °C. After 1 h of reaction time the suspension was transferred into a polyethylene vial and placed on a shaker at 23 °C in a constant temperature room. Sub-samples were taken after 1 day, 1 week, 1 month, 9 months and 1 year.

2.3. Mineralogical and chemical analyses

2.3.1. Solid phases

Time-resolved *in situ* Raman spectra of the reactive suspension were collected every 62 seconds with a Raman RXN2^{TM} analyzer from Kaiser Optical Systems equipped with a quarter-inch immersion optic Kaiser MR probe. The Raman spectra were recorded in the 100–3425 cm^{-1} region with a resolution of 1 cm^{-1} using a 785 nm laser beam with an exposure time of 60 sec. Powder X-ray diffraction (XRD) patterns of the solid phases collected at certain reaction times (see Table 1) were recorded by a PANalytical X'Pert PRO diffractometer using Co-Kα-radiation (40 mA, 40 kV) at a 2θ range from 5° to 85° and a scan speed of 0.03° s^{-1}. For qualitative characterization of the crystalline products the PANalytical HighScore Plus software with the ICSD database was used. Note here, the detection limit of crystalline phases is ~1 wt%. Infrared spectra of the solids in the range of 650–4000 cm^{-1} were collected using a Perkin Elmer Spektrum 100 Attenuated Total Reflectance-Fourier Transform Infrared (ATR-FTIR) spectrometer with a resolution of 4 cm^{-1}. Selected precipitates were gold-coated and imaged using a ZEISS DSM 982 Gemini scanning electron microscope (SEM) equipped with a field emission gun operating at 2 kV accelerating voltage.

Additionally, subsamples of selected crystalline solids were embedded in a two-component epoxy resin, polished, carbon coated and analyzed with an electron probe

Table 1
Chemical composition of reactive solutions and solids and mineral composition of the precipitates at certain reaction times. The term "calculated" refers to Mg and SO_4 content of the solid estimated using Eqs. (2) and (3) whereas the term "measured" refers to the bulk solid composition measured after solid digestion.

Sample	Time (min)	pH	Alkalinity (mM)	Solution (mM)			Solid				
				Ca	Mg	SO_4	Mg mol% calculated	Mg mol% measured	SO_4 mol% calculated	SO_4 mol% measured	XRD/Raman
s0_initial		7.98	99	–	26.2	–					
s0_1	0.2	8.34	107	6.2	25.1	–	0.4	1.6	–	–	ACC
s0_2	2.3	8.32	108	6.5	24.5	–	0.6	1.7	–	–	ACC
s0_3	5.2	8.31	106	6.3	24.3	–	0.7	1.9	–	–	ACC
s0_4	7.8	8.30	104	6.2	24.1	–	0.8	2.0	–	–	ACC
s0_5	10.7	8.30	102	5.7	22.1	–	1.5	2.6	–	–	ACC
s0_6	13.1	8.29	92	4.8	16.1	–	3.6	4.2	–	–	ACC, HMC
s0_7	16.0	8.30	78	2.8	8.3	–	6.1	6.5	–	–	ACC, HMC
s0_8	22.1	8.32	68	0.8	3.3	–	7.6	8.0	–	–	ACC, HMC
s0_9	30.8	8.33	65	0.4	2.4	–	7.8	8.2	–	–	ACC, HMC
s0_10	39.9	8.38	65	0.2	2.4	–	7.9	8.2	–	–	HMC
s0_11	62.4	8.51	64	0.2	2.3	–	7.9	8.3	–	–	HMC
s0_12	1434.0	8.52	60	0.1	0.9	–	8.3	8.6	–	–	HMC
s0_13	18960.0	8.67	60	0.1	0.2	–	8.5	8.8	–	–	HMC
s0_14	51900.0	8.72	60	0.1	0.2	–	8.5	9.0	–	–	HMC
s0_15	162720.0	8.88	59	0.1	0.3	–	8.5	9.0	–	–	HMC
s0_16	400320.0	9.05	59	0.3	0.2	–	8.5	9.1	–	–	HMC
s0_17	531360.0	9.16	61	0.1	0.1	–	8.6	9.0	–	–	HMC
s10_initial		7.99	99	–	27.2	9.4					
s10_1	0.2	8.35	109	6.5	25.8	9.3	0.5	1.4	0.0	0.2	ACC
s10_2	2.2	8.33	107	6.8	25.2	9.3	0.7	1.6	0.0	0.2	ACC
s10_3	4.3	8.33	106	6.8	25.0	9.3	0.8	1.7	0.0	0.2	ACC
s10_4	7.3	8.31	106	6.5	24.9	9.4	0.8	2.1	0.0	0.3	ACC
s10_5	9.9	8.30	101	6.3	23.7	9.3	1.3	2.2	0.0	0.3	ACC
s10_6	12.5	8.27	92	5.4	17.5	9.0	3.4	3.8	0.1	0.3	ACC, HMC
s10_7	15.1	8.24	81	3.3	10.8	8.5	5.6	5.5	0.3	0.3	ACC, HMC
s10_8	21.2	8.31	71	1.1	4.9	8.2	7.4	7.5	0.4	0.3	ACC, HMC
s10_9	30.4	8.32	67	0.5	3.7	8.2	7.8	7.8	0.4	0.3	ACC, HMC
s10_10	39.5	8.35	66	0.3	3.6	8.2	7.8	7.8	0.4	0.3	HMC
s10_11	62.3	8.46	66	0.2	3.4	8.2	7.8	7.8	0.4	0.3	HMC
s10_12	1414.0	8.51	66	0.1	1.7	8.4	8.4	8.3	0.3	0.2	HMC
s10_13	17520.0	8.57	60	0.1	0.5	8.4	8.7	8.7	0.3	0.2	HMC
s10_14	50460.0	8.66	60	0.0	0.3	8.5	8.8	8.8	0.3	0.2	HMC
s10_15	–	–	–	–	–	–	–	–	–	–	–
s10_16	398880.0	9.01	59	0.1	0.1	9.0	8.8	9.0	0.1	0.2	HMC
s10_17	529920.0	9.12	61	0.1	0.0	8.6	8.8	8.9	0.2	0.2	HMC
s30_initial		7.99	99	–	26.8	26.8					
s30_1	0.3	8.385	110	6.6	25.9	26.6	0.4	1.7	0.1	1.0	ACC

s30_2	2.2	8.374	109	7.3	25.4	26.6	0.5	1.5	0.0	0.6	ACC
s30_3	4.0	8.371	108	7.1	25.2	26.7	0.6	1.5	0.0	0.7	ACC
s30_4	6.9	8.343	106	7.0	24.8	26.6	0.8	1.7	0.1	0.7	ACC
s30_5	9.9	8.295	100	6.3	21.0	26.4	2.1	2.7	0.1	0.7	ACC, HMC
s30_6	12.0	8.298	90	4.6	14.2	25.5	4.4	4.5	0.4	0.7	ACC, HMC
s30_7	14.9	8.299	77	2.8	8.3	24.6	6.3	6.5	0.7	1.0	ACC, HMC
s30_8	21.1	8.305	71	1.0	4.4	24.0	7.4	7.6	0.9	1.0	ACC, HMC
s30_9	30.2	8.326	69	0.5	3.7	24.0	7.6	7.8	0.9	0.7	ACC, HMC
s30_10	38.7	8.365	70	0.3	3.7	24.0	7.6	7.8	0.9	0.9	HMC
s30_11	62.3	8.483	68	0.2	3.6	24.1	7.7	7.8	0.9	0.9	HMC
s30_12	1420.0	8.5	64	0.1	1.8	24.2	8.2	8.4	0.8	0.5	HMC
s30_13	13200.0	8.56	60	0.2	0.3	24.9	8.7	8.7	0.6	0.5	HMC
s30_14	46140.0	8.58	62	0.1	0.1	25.0	8.7	8.9	0.6	0.5	HMC
s30_15	–	–	–	–	–	–	–	–	–	–	–
s30_16	394560.0	8.98	59	0.0	0.1	25.4	8.7	9.2	0.4	0.5	HMC
s30_17	525600.0	9.11	60	0.0	0.2	25.3	8.7	9.0	0.5	0.5	HMC
s30_2_initial		7.98	99	0.0	27.1	27.3					
s30_2_1	0.2	8.39	108	6.6	25.8	27.1	0.5	1.3	0.1	0.6	ACC
s30_2_2	2.2	8.37	109	6.9	25.4	27.3	0.6	1.7	0.0	0.9	ACC
s30_2_3	4.1	8.37	109	6.8	25.1	27.2	0.8	1.7	0.0	0.9	ACC
s30_2_4	6.9	8.33	107	6.9	24.5	27.2	0.9	2.0	0.1	1.0	ACC
s30_2_5	10.0	8.30	96	5.6	18.9	26.5	2.9	3.4	0.3	1.0	ACC, HMC
s30_2_6	12.5	8.30	85	3.5	10.9	25.5	5.5	5.3	0.6	0.9	ACC, HMC
s30_2_7	15.0	8.30	77	2.3	6.9	24.9	6.8	6.7	0.8	0.9	ACC, HMC
s30_2_8	21.3	8.30	71	1.0	3.9	24.4	7.7	7.7	1.0	1.0	ACC, HMC
s30_2_9	30.3	8.33	69	0.4	3.4	24.5	7.9	7.7	0.9	1.0	ACC, HMC
s30_2_10	39.9	8.37	67	0.3	3.3	24.6	7.9	7.8	0.9	1.0	HMC
s30_2_11	62.4	8.48	68	0.2	3.3	24.6	7.9	7.8	0.9	0.9	HMC
s30_2_12	1415.0	8.53	64	0.2	1.5	24.8	8.4	8.3	0.8	0.5	HMC
s30_2_13	16080.0	8.60	60	0.0	0.5	25.2	8.7	8.7	0.7	0.5	HMC
s30_2_14	49020.0	8.68	62	0.0	0.3	25.5	8.8	8.8	0.6	0.5	HMC
s30_2_15	–	–	–	–	–	–	–	–	–	–	–
s30_2_16	397440.0	9.05	63	0.1	0.1	26.4	8.8	9.0	0.3	0.5	HMC
s30_2_17	528480.0	9.18	64	0.0	0.1	27.0	8.8	8.9	0.1	0.5	HMC
s45_initial		8.07	99	–	27.0	45.9					
s45_1	0.2	8.45	109	–	25.1	41.8	–	1.5	–	1.5	ACC
s45_2	2.2	8.43	109	7.1	25.1	45.7	0.7	1.7	0.1	1.6	ACC
s45_3	4.3	8.43	110	7.2	25.1	45.8	0.7	1.5	0.0	1.3	ACC
s45_4	7.0	8.41	109	7.5	24.7	46.1	0.8	1.6	−0.1	1.2	ACC
s45_5	9.9	8.29	101	6.6	20.5	45.4	2.3	3.0	0.2	1.5	ACC, HMC
s45_6	12.7	8.30	83	3.5	10.1	42.7	5.7	5.5	1.1	1.5	ACC, HMC
s45_7	15.2	8.30	77	2.1	6.8	42.0	6.8	6.8	1.3	1.5	ACC, HMC
s45_8	21.1	8.33	73	0.8	4.8	41.6	7.4	7.4	1.4	1.6	ACC, HMC
s45_9	30.3	8.32	71	0.4	4.6	41.9	7.4	7.4	1.3	1.7	ACC, HMC
s45_10	38.9	8.36	71	0.7	4.6	41.8	7.4	7.4	1.4	1.8	HMC
s45_11	61.1	8.46	70	0.3	4.3	41.9	7.5	7.5	1.3	1.6	HMC

s45_12	1420.0	8.51	68	0.1	2.1	42.2	8.2	8.2	1.2	0.8	HMC
s75_initial		7.98	101	–	26.9	74.3					
s75_1	0.2	8.46	112	7.3	25.9	73.9	0.3	1.5	0.2	2.4	ACC
s75_2	2.1	8.45	112	7.7	25.4	74.1	0.5	1.4	0.1	2.0	ACC
s75_3	4.1	8.45	110	7.7	25.3	74.1	0.6	1.7	0.1	2.6	ACC
s75_4	7.0	8.41	110	7.6	24.4	73.7	0.9	1.9	0.2	2.7	ACC
s75_5	9.9	8.25	96	6.4	16.6	71.6	3.6	3.8	1.0	2.4	ACC, HMC
s75_6	12.0	8.30	88	3.9	11.0	69.9	5.4	5.5	1.5	2.1	ACC, HMC
s75_7	15.0	8.30	79	2.3	7.7	68.7	6.5	6.6	1.9	2.3	ACC, HMC
s75_8	21.1	8.32	76	0.9	6.0	67.8	7.0	7.0	2.2	2.6	ACC, HMC
s75_9	30.2	8.32	75	0.6	5.9	67.8	7.0	7.0	2.2	2.3	ACC, HMC
s75_10	39.3	8.37	74	0.4	5.8	68.1	7.0	7.0	2.1	2.6	HMC
s75_11	62.4	8.48	71	0.2	5.7	68.4	7.0	7.1	2.0	2.5	HMC
s75_12	1405.0	8.48	67	0.1	3.6	68.2	7.7	7.8	2.0	1.3	HMC
s75_13	14640.0	8.52	63	0.1	1.3	69.1	8.4	8.4	1.7	1.4	HMC
s75_14	47580.0	8.57	63	0.1	0.7	69.5	8.6	8.7	1.6	1.2	HMC
s75_15	158400.0	8.77	62	0.4	0.3	69.7	8.7	8.9	1.5	1.1	HMC
s75_16	396000.0	9.02	60	0.0	0.1	70.9	8.7	9.1	1.1	1.2	HMC
s75_17	527040.0	9.14	62	0.0	0.1	71.3	8.7	9.0	1.0	1.1	HMC
s90_initial		8.03	100	–	27.1	92.0					
s90_1	0.2	8.52	110	7.4	25.4	90.1	0.6	1.3	–	2.7	ACC
s90_2	2.2	8.51	111	8.1	25.4	91.9	0.6	1.4	0.0	2.5	ACC
s90_3	4.1	8.49	112	7.9	25.2	92.3	0.7	1.5	−0.1	2.9	ACC
s90_4	6.9	8.40	109	7.9	24.1	91.8	1.1	1.8	0.1	2.7	ACC
s90_5	10.0	8.26	92	5.3	14.1	88.1	4.5	4.5	1.3	3.0	ACC, HMC
s90_6	12.3	8.31	83	3.2	9.1	86.1	6.1	6.1	2.0	2.5	ACC, HMC
s90_7	14.9	8.31	79	1.9	7.1	85.5	6.7	6.7	2.2	3.0	ACC, HMC
s90_8	21.1	8.33	76	0.8	6.1	84.8	7.0	6.9	2.4	3.1	ACC, HMC
s90_9	30.3	8.34	75	0.5	6.0	85.2	7.0	6.9	2.3	2.9	ACC, HMC
s90_10	39.1	8.37	73	0.3	5.8	85.3	7.1	6.9	2.2	3.0	HMC
s90_11	61.4	8.46	74	0.3	5.7	85.6	7.1	7.0	2.1	2.9	HMC
s90_12	1430.0	8.51	70	0.2	3.0	85.2	7.9	7.9	2.2	1.4	HMC
s90_13	13440.0	8.54	63	0.1	1.1	86.9	8.5	8.4	1.7	1.4	HMC
s90_14	46380.0	8.61	62	0.0	0.3	87.5	8.7	8.7	1.5	1.5	HMC
s90_15	–	–	–	–	–	–	–	–	–	–	–
s90_16	394800.0	9.08	60	0.0	0.1	90.8	8.8	9.0	0.4	1.4	HMC
s90_17	525840.0	9.20	63	0.0	0.1	91.1	8.8	8.9	0.3	1.2	HMC

ACC. . .amorphous calcium carbonate.
HMC. . .high-Mg calcite.

microanalysis (EPMA) using a JEOL JXA8530F Plus Hyper Probe equipped with a field emission gun. Secondary electron (SEI) and back-scattered electron (BSE) images were recorded at an accelerating voltage of 10 kV and 2 nA. Furthermore, (semi)-quantitative high-resolution element distribution images of Ca, Mg and S were recorded using the wave-dispersive analytical mode (WDS), an acceleration voltage of 10 kV and 5 nA and a dwell time of 30 mS. Element quantifications were performed against mineral standards from SPI (Calcite for Ca, Dolomite for Mg and Barite for S). From these images, average Mg and S (given as SO_4) contents in solid samples were calculated using data of 100 × 100 pixel (Table S2).

2.3.2. Reactive solutions

The pH of the reactive solution was measured *in situ* with a SI Analytics Silamid® gel electrode coupled to a SI Analytics TitroLine® 7800. The electrode was calibrated on the activity scale with NIST standard buffer solutions at pH 4.01, 7.00 and 10.00 (analytical uncertainty ±0.03 units). Total alkalinity was determined by a Schott TitroLine alpha plus titrator using a 10 mM HCl solution with an analytical precision of ±2%. Aqueous Ca, Mg and SO_4 concentrations were measured by Ion Chromatography (IC) using a Dionex IC S 3000 with IonPac® AS19 and CS16 column with an analytical precision of ±3%. The distribution of aqueous species in the reactive solution and saturation indices (SI) with respect to amorphous and crystalline phases were calculated using the PHREEQC software in combination with its minteq.v4 database modified by the addition of the solubility products for ACC (Brečević and Nielsen, 1989), hydromagnesite (Gautier et al., 2014), nesquehonite, dypingite (Harrison et al., 2019) and bassanite (Shen et al., 2019). In order to calculate SI (SI = IAP/K_{sp}) of the amorphous solids that are enriched in Mg, the ion activity product (IAP) was calculated using the equation

$$IAP = (a_{Ca^{2+}})^{1-x}(a_{Mg^{2+}})^{x}(a_{CO_3^{2+}}) \quad (1)$$

where a_x denotes the activities of free ions in solution and the solubility product (K_{sp}) of ACC containing 0.6 mol % Mg was calculated using the equation given by Purgstaller et al. (2019). The SO_4 content of ACC accounted for ≤0.1 mol% and was therefore not considered in the calculation of the ion activity product.

2.3.3. Chemical composition of solid phases

The Mg and SO_4 contents of the solids (in mol%) were calculated by mass balancing the reactive solution sampled at certain time steps (Table 1) and according to the equations

$$[Mg]_{solid}(mol\%) = \frac{n_{Mg}}{n_{Mg} + n_{Ca}} \times 100 \quad (2)$$

and

$$[SO_4]_{solid}(mol\%) = \frac{n_{SO_4}}{n_{Mg} + n_{Ca}} \times 100 \quad (3)$$

where n_{Mg}, n_{Ca} and n_{SO4} denote the moles of Mg, Ca and SO_4 in the solid phase. The moles of each element/molecule in the solid phase (n_X) was calculated at each time step by the subtraction of the actual measured Ca, Mg and SO_4 concentrations from the total available Ca, Mg and SO_4 concentrations in mol/L. The total available concentration of Ca was derived from 1.5 g ACC ($CaCO_3{\cdot}0.4H_2O$; Konrad et al., 2016) with a molecular weight of 107.3 g/mol converted into mol/L whereas total available concentrations of Mg and SO_4 were derived by their initial concentrations (mol/L) in the reactor prior to the introduction of ACC. The sum of the cations n_{Mg} + n_{Ca} represents the sum of the anions n_{SO4} + n_{CO3}. No correction for the amount of sampled material (solid + solution) in the course of the experimental runs was applied because the suspension was sampled homogeneously. Additionally, the elemental content of digested bulk solids (i.e. Ca, Mg and SO_4) was measured by IC following the protocol described in Goetschl et al. (2019). Note here that the elemental contents of the crystalline phase derived from both approaches are in excellent agreement, whereas the elemental composition of the amorphous phase exhibits higher values in the case of the measurement by IC (see Table 1).

3. RESULTS

3.1. Temporal evolution of ACC transformation to HMC

The *in situ* Raman spectra indicate that the transformation of ACC into HMC was initiated within a few minutes after its introduction into the HCO_3-Mg-(SO_4-)bearing solution (e.g. experiment s30 in Fig. S1). Note here that just before introducing ACC, the Raman spectra of the initial reactive solution depicts vibration bands of aqueous HCO_3^- and SO_4^{2-} at 1017 cm^{-1} and 981 cm^{-1}, respectively (Davis and Oliver, 1972; Fujita and Kimura, 1981; Wang et al., 2005). The band intensities of aqueous HCO_3^- and SO_4^{2-} are decreasing rapidly in 2 steps during the course of the experiments, correlating with the addition of ACC in the reactor and its transformation to HMC. Immediately after ACC was added to the reactive solution, the recorded Raman spectra exhibit the characteristic broad $\nu_1(CO_3)$ ACC band at 1080 cm^{-1} (Wang et al., 2012), suggesting that this phase is the only solid present in the reactor within the first 10 min of the experiments. The intensity of the ACC $\nu_1(CO_3)$ band progressively decreases after ~5 min of reaction time, indicating the dissolution of the amorphous phase. Subsequently, the $\nu_1(CO_3)$ band at 1087–1088 cm^{-1}, characteristic for HMC (Bischoff et al., 1985), exhibits a strong intensity increase that is accompanied by band sharpening (Fig. S1). The intensity maximum (I_{max}) of the $\nu_1(CO_3)$ band is observed at 1088 cm^{-1} in experiments conducted in the absence of SO_4 (i.e. s0) and in the presence of 10 mM SO_4 (i.e. s10). In experiments performed at higher SO_4 concentrations of 30, 45, 75 and 90 mM SO_4 (i.e. s30, s45, s75 and s90), the I_{max} of the $\nu_1(CO_3)$ band is observed at 1087 cm^{-1}. After about 20–25 min of reaction time the intensity of the $\nu_1(CO_3)$ band of HMC (1087–1088 cm^{-1}) reaches a plateau (Fig. S2). Thus in all the experimental runs the temporal evolution of the transformation from ACC into HMC follows the same pattern and can be roughly divided into three stages (Fig. 2): (I)

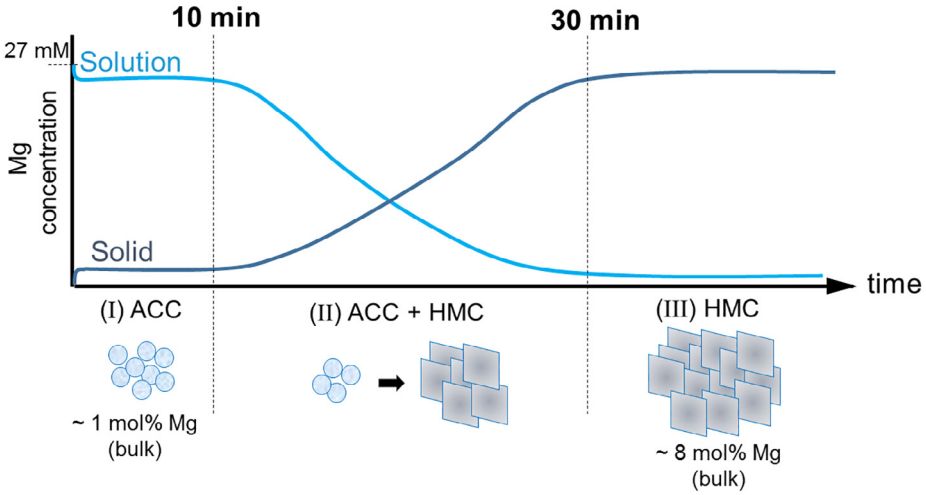

Fig. 2. Simplified illustration of the mineralogical and chemical evolution as a function of reaction time. The light blue line refers to the Mg concentration of the reactive solution and the dark blue line refers to the Mg content of the solid phase. The evolution can be divided in 3 different stages: (I) ACC stable – exchange of solutes between ACC and reactive solution, (II) ACC transformation to HMC via dissolution and re-precipitation, (III) HMC stable – continuous exchange of solutes between HMC and reactive solution. (For interpretation of the references to color in this figure legend, the reader is referred to the web version of this article.)

$\leq$ about 10 min, ACC occurrs as the only phase; (II) between about 10 to 30 min, ACC co-exists with HMC; (III) $\geq$ about 30 min, HMC is the only solid phase. More details about the exact onset of stage II in each individual experimental run are described in the following paragraph.

Actually, the timepoint at which the intensity increase of the $\nu_1(CO_3)$ band occurs - indicative of the onset of HMC formation - appears to be a function of the $MgSO_4^0$ concentration of the reactive solution. Note here that the intensity increase of the $\nu_1(CO_3)$ band is marking the transition from stage I to stage II in the experimental runs. The time of the intensity increase of the intensity maximum (I_{max}) of the $\nu_1(CO_3)$ band for all experiments can be seen in Fig. S2. In the absence of SO_4 the intensity of the $\nu_1(CO_3)$ band increases after 12.4 min of reaction time, whereas in experiment s90 the intensity of the $\nu_1(CO_3)$ band increases already after 8.3 min of reaction time. Actually, as it can be seen in Fig. 3A, a linear correlation between $MgSO_4^0$ (determined by initial SO_4) concentration and the time of onset of HMC formation exists and can be described by the linear equation

$$\text{time (min)} = -0.3840(\pm 0.0455) \times MgSO_4{}^0\ (\text{mM}) + 12.0430(\pm 0.2480); R^2 = 0.92 \quad (4)$$

where reaction *time* is given in minutes and $MgSO_4^0$ denotes concentration in mM of the reactive solution. The inverse trend is observed when the time of the $\nu_1(CO_3)$ band intensity increase is plotted as a function of free Mg^{2+} concentration (Fig. 3B).

The XRD analyses of the solid phases collected during the experimental runs (see Table 1) are in excellent agreement with the observations of the *in situ* Raman measurements. The XRD patterns of samples collected within 7 min of reaction time are consistent with the initial synthetic ACC. The first characteristic HMC peaks are observed in the diffractograms of samples collected at about 10 min of reaction time (e.g. experiment s30 in Fig. S3). Note here that the *in situ* Raman measurements reflect a more precise time of the onset of HMC formation due to the higher temporal resolution of data collection compared to XRD measurements. Comparing the XRD patterns of the HMCs formed via ACC to a pattern of pure calcite reference material ($CaCO_3 \geq 99\%$, p.a. from Roth), the main calcite peak (104) is significantly lower in intensity, it occurs with an extended full width at half maximum (FWHM) and is shifted to a higher 2θ position by +0.25° (±0.03°) indicative of its Mg content. Note here that the peak positions of the newly precipitated HMCs analyzed at time steps from 10-62 min (Fig. S3) do not differ significantly from each other, indicating similar Mg contents of calcite (Goldsmith et al., 1961; Milliman et al., 1971). No significant peak shifts towards higher 2θ positions of the analyzed HMCs have been observed as a function of experimental reaction time up to 1 year.

The formation of HMC is further confirmed by ATR-FTIR analyses of collected solids. As it can be seen in Fig. 4, the FTIR spectra of ACC are characterized by carbonate vibration bands ν_1 and ν_2 at 1075 and 860 cm^{-1} (Andersen and Brečević, 1991; Loste et al., 2003; Konrad et al., 2018), while the HMC exhibits ν_1, ν_2, and ν_4 bands at 1086, 870/848 and 714 cm^{-1} (White, 1974; Böttcher et al., 1997). Previous studies have shown that the shift of the infrared (CO_3)-bands towards higher or lower wavenumbers is associated with increasing Mg^{2+} substitution (Böttcher et al, 1997; Huang et al., 2018). Moreover, FTIR spectra of the solids that have been collected from experiments performed in the presence of SO_4 - e.g. experiment s75 in Fig. 4 - exhibit additional bands next to the characteristic carbonate bands. In the case of ACC

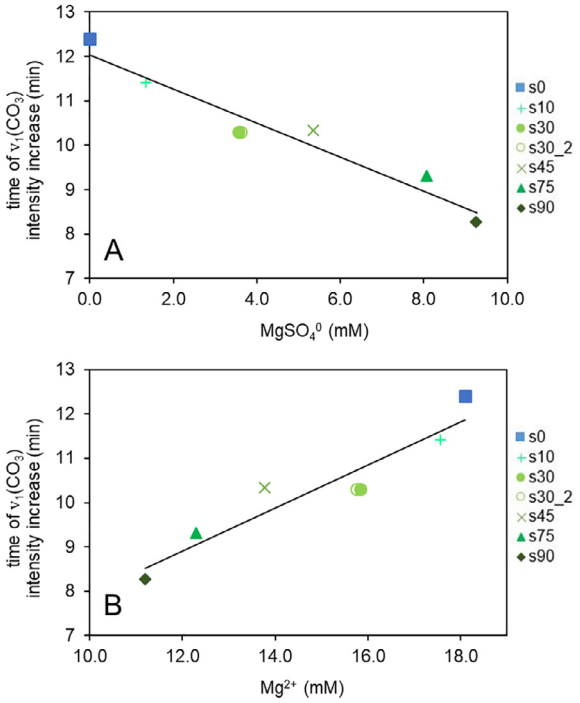

Fig. 3. Time of intensity increase of the intensity maximum (I_{max}) of the $(CO_3)_{solid}$ ν_1 band for all experiments obtained using *in situ* Raman spectroscopy. The formation of HMC is indicated by the rapid increase of I_{max} between 8.3 and 12.4 min of reaction time (Fig. S2). A) Elevated $MgSO_4^0$ concentrations of the reactive solution (referring to initial SO_4 concentrations) cause an earlier start of HMC formation B) Elevated Mg^{2+}(aq) concentrations at lower sulfate concentrations induce a longer induction time and therefore prolonged metastability of ACC.

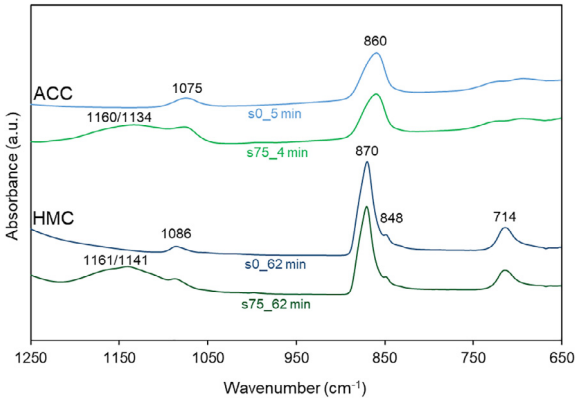

Fig. 4. FTIR spectra from experiments in the absence of sulfate (s0 - blue) and in the presence of 75 mM sulfate (s75 - green) after ~5 min and ~1 h of reaction time, respectively. (For interpretation of the references to color in this figure legend, the reader is referred to the web version of this article.)

(s75_4 min) an additional broad band at 1134 cm^{-1} appears including a shoulder at ~1160 cm^{-1}, and in the case of HMC (s75_62 min) two additional bands at 1141 and 1161 cm^{-1} are visible (Fig. 4). These additional bands can be ascribed to internal ν_3 vibrations of SO_4 (Takano et al., 1980; Aizenberg et al., 2002; Floquet et al., 2015; Balan et al., 2017).

Scanning Electron Microscopy (SEM) observations reveal that synthetic ACC particles that occur as spheres with an average diameter of 90 nm, transformed into HMCs that occur as nanocrystalline aggregates (Fig. 5A). The surface of the HMC aggregates displays numerous idiomorphic, rhombohedral calcite crystals that are interlocked into each other. No significant differences in the crystal morphology of the HMCs, formed in the absence or presence of SO_4, have been observed. Similarly, no changes of the crystal morphology as a function of time, even after 1 year of reaction time, were observed (Fig. S4).

Microphotographs of cross sections of the nanocrystalline HMC aggregates reveal their inner microstructure which appears as radially oriented columns (Fig. 5B). The columns become thicker from the inside out. The rough surface and disrupted centers after thick section polishing indicate a high internal porosity of ACC-derived HMC. Comparing the inner structure of precipitates collected after 1 h to the ones collected after 1 year the latter exhibit a more dense and solid microstructure (Fig. S5).

3.2. Chemical evolution of the reactive solution

The chemical composition of the reactive solution prior to ACC addition in the reactors, and during the first 30 min of the experimental runs, is illustrated in Fig. 6 (see data in Table 1). The same three stages that are specified by solid characterization, which are described above, can be identified by the temporal evolution of the reactive solution. Note here that the chemical evolution of the reactive solution points towards an ~5 min earlier onset of stage II compared to the solid characterization. The ACC transformation, which is indicated by the pH decrease, occurs in the latter case between 3 and 7 min of reaction time (Table 1; Fig. S6) instead of 8 and 12 min that is observed by *in situ* Raman spectra. It is thus evident that the onset of solid transformation is followed more accurately using the solution composition in contrast to the use of *in situ* Raman spectroscopy which is limited by the detection limit of the method for solid identification. Nevertheless, the kinetics of ACC transformation based on solution chemistry are in accordance with the observations by solid characterization and exhibit the same trend as a function of initial SO_4 concentration.

The evolution of aqueous Ca concentration (Fig. 6A) and alkalinity (Table 1) of the reactive solution is characterized by a sudden concentration increase caused by ACC addition into the reactor (stage I). The Ca concentrations increase from zero to ~6–8 mM, and remain almost constant during stage I until ACC transformation to HMC was initiated. The alkalinity concentrations increase from ~100 to 107–112 mM and remain almost constant up to 4–7 min of reaction time. This first stage is followed by a substantial and rapid decrease of Ca concentration in the reactive solutions corresponding to HMC formation (stage II). During stage II the Ca concentrations drop to lower values within 30 min of reaction time, in all experiments. The alkalinity concentrations level off achieving steady state

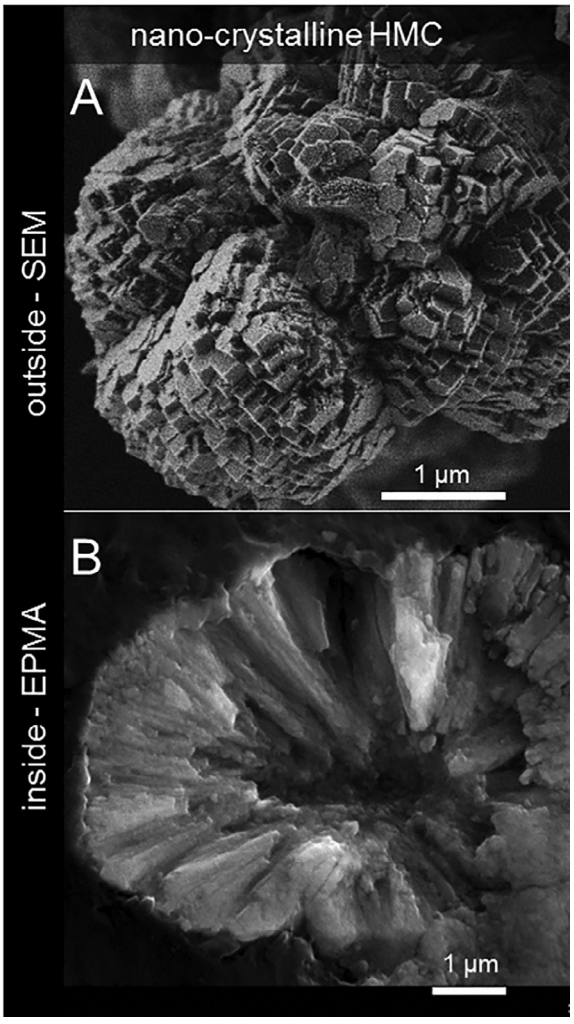

Fig. 5. A) SEM photograph of HMC (experiment s75) shows the outer appearance of the nano-crystalline product after ACC transformation. B) EPMA BSE-image shows the inner microstructure of the nano-crystalline HMC aggregate (experiment s90).

concentrations with values between ~65 and 75 mM depending on the SO_4 concentration of each run (see Table 1). The initial increase in Ca and alkalinity concentrations immediately after the addition of ACC into the reactors can be assigned to the rapid dissolution of the amorphous solid. Indeed, the SI_{ACC*} values document that the reactive solution achieves rapidly chemical equilibrium with respect to ACC (SI_{ACC*} about 0; see Fig. 6C and Table S1). The positive correlation between total Ca and SO_4 concentrations of the reactive solution during stage I points towards enhanced ACC dissolution with increasing SO_4 concentration, which is also indicated by the positive correlation between pH and SO_4 concentration during stage I (Fig. S6). The release of Ca into the solution, however, results in increasing oversaturation with respect to other $CaCO_3$ polymorphs, such as calcite and aragonite, as it can be seen in Table S1. Note that although during stage I and up to 10 min of reaction time the reactive solutions are supersaturated with respect to hydromagnesite ($Mg_5(CO_3)_4(OH)_2{\cdot}4H_2O$), this mineral phase is not detected by mineralogical analyses. Other hydrated Mg-carbonate phases such as nesquehonite ($MgCO_3{\cdot}3H_2O$) and dypingite ($Mg_5(CO_3)_4(OH)_2{\cdot}8H_2O$) are undersaturated in all the reactive solutions as well as gypsum ($CaSO_4{\cdot}2H_2O$) and bassanite ($CaSO_4{\cdot}0.5H_2O$) (see Table S1).

In Fig. 6B, it can be seen that in all experimental runs, the initial aqueous Mg concentration (~27 mM) decreases slightly to ~25 mM immediately after the introduction of ACC in the reactors and remains quasi constant during stage I until the onset of the ACC transformation. During the transformation of ACC to HMC (stage II) the temporal evolution of Mg concentration in the reactive solution exhibits a behaviour similar to that of Ca. Up to ~22 min of reaction time the aqueous Mg concentration is reduced rapidly to ~3–6 mM and drops afterwards at a slower rate towards zero values until the end of the experimental runs after 1 year. In experiments containing SO_4, the temporal evolution of SO_4 concentrations follows the same pattern as Mg concentrations in stage I and II (Table 1). After ACC was introduced into the reactors the SO_4 concentrations decrease slightly (stage I) and drop significantly during the transformation (stage II). In contrast to the behaviour of Mg, the SO_4 concentrations increase continuously during stage III until the end of the experiments after 1 year.

Speciation calculations indicate that concentrations of free aqueous Ca^{2+} and Mg^{2+} ions account for 60–35% and 75–45% of their total concentrations respectively, depending on the SO_4 concentration in each experiment (Table S1). The abundance of both Ca^{2+} and Mg^{2+} decreases with increasing SO_4 concentration. In particular, the prevailing Mg^{2+}/Ca^{2+} ratio of the reactive solution (Table S1) follows a clear trend as a function of SO_4 concentration and is decreasing slightly with increasing SO_4 concentrations during stages I and II. However, the Mg^{2+}/Ca^{2+} ratio of the reactive solutions remains almost constant during the ACC transformation and abruptly levels up to higher values towards the end of stage II after 15–20 min of reaction time.

Apparent precipitation rates (r_i) were calculated from the first derivative of the sum of Ca^{2+} and Mg^{2+} concentration of the reactive solution with respect to time, from the onset of ACC transformation to the attainment of quasi constant aqueous concentrations, using the equation

$$r_i = \frac{dc_{(Ca^{2+}+Mg^{2+})}}{dt} \quad (5)$$

where $c^{2+}_{\in Mg}$ stands for the sum of Ca^{2+} and Mg^{2+} concentrations in the reactive solution and t designates time. In this study, the apparent precipitation rate (r_i) describes the transfer of ions from the reactive solution to the crystalline solid phase during stage II (sub-samples collected within the time interval of 4 to 22 min). Note here that r_i refers to bulk composition of precipitated solid during stage II without considering proportion of amorphous and crystalline material. The calculated precipitation rates are presented in Table 2 and plotted in Fig. 7. The obtained results suggest that there is a linear correlation between the apparent precipitation rate during stage II and the ini-

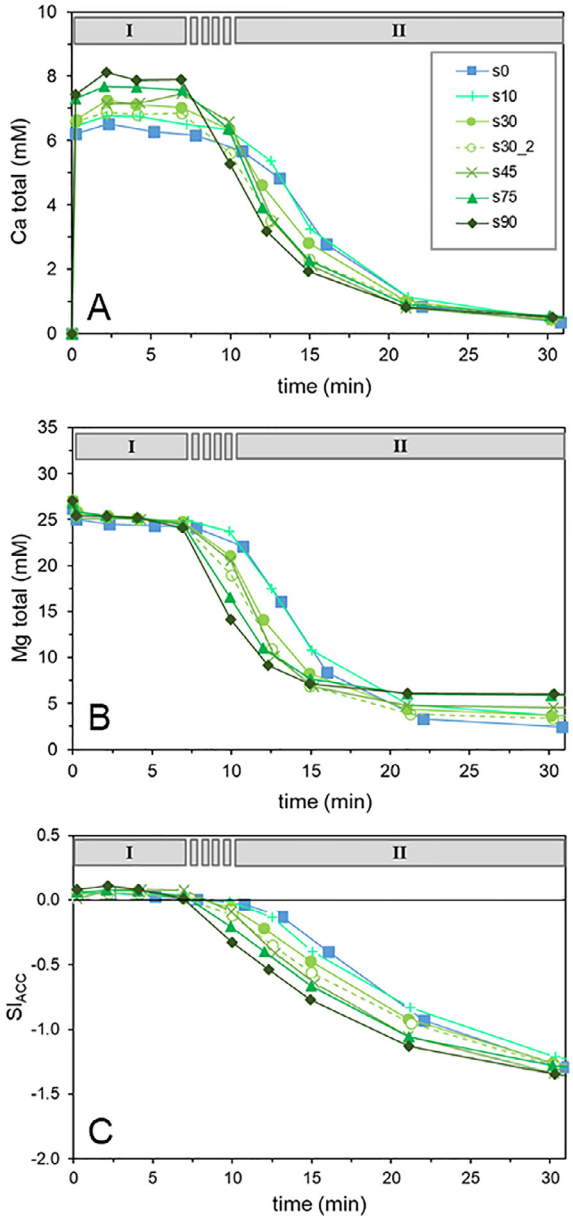

Fig. 6. A, B) Temporal evolution of the Ca and Mg concentration of the reactive solution and C) saturation indices (SI) in respect to ACC containing 0.6 mol% Mg within 30 min of reaction time – stage (I) and (II).

tial SO_4 concentration of the reactive solution that can be described by the linear equation

$$r_i\ (\mathrm{mM/min}) = -0.0055(\pm 0.0003) \times SO_4\ (\mathrm{mM}) + 1.2184(\pm 0.0157); R^2 = 0.98 \quad (6)$$

The precipitation rate during the ACC transformation (stage II) was lower when the SO_4 concentration was higher.

The temporal evolution of Mg and SO_4 in the reactive solutions displayed as cumulative loss (in %) can be seen in Fig. 8. The results show a continuous decrease of Mg concentration and a continuous increase of SO_4 concentration in the reactive solution during stage III where HMC is the only mineral present. Notably, after 1 month of reaction time the Mg concentration of the reactive solution decreases already about 99% compared to its initial concentration in the reactors.

3.3. Chemical evolution of solid phases

After ACC is introduced into the solution, it instantly uptakes Mg and SO_4 (Table 1). Actually, in all the experiments within the first 4 min of reaction time (stage I), the Mg content of ACC is 0.6 ± 0.2 mol%. The SO_4 content of ACC lies within 0 and 0.1 mol% for all amorphous solid samples and does not exhibit a significant trend as a function of SO_4 concentration or reaction time. The Mg content of ACC is independent from the initial SO_4 concentration in the reactive solution, as well as from the SO_4 content of the ACC, which is shown in Fig. 9A.

After the onset of ACC transformation (stage II), a rapid increase of Mg and SO_4 contents of the solids is observed. After 1 h of reaction time (stage III), HMC is the only solid phase that was identified. The Mg content of this calcite is ranging from 7 to 8 mol% and SO_4 content from 0 to 2 mol%. The Mg content of calcite formed via ACC exhibits a linear anticorrelation with its SO_4 content, whereas the SO_4 content is positively correlated with the initial SO_4 concentration of the reactive solution (Fig. 9B). During stage III, the Mg content of calcite is continuously increasing whereas its SO_4 content is continuously decreasing (Table 1).

High-resolution element distribution images of cross-sectioned HMC aggregates collected after 1 day and 1 year of reaction time show a homogeneous distribution of Mg and SO_4 (represented by S) within and between the HMC aggregates (Fig. 10 and Fig. S7). The average contents of Ca, Mg and SO_4 are calculated in mol% and listed in Table S2. The extent of Mg and SO_4 contents estimated by WDS analysis of selected HMC samples is in reasonable agreement with the elemental contents estimated by mass balance calculation and bulk measurement after solid digestion.

4. DISCUSSION

4.1. Reactivity of ACC

An interesting feature observed in this study is the change in the chemical composition of the amorphous phase as soon as it comes in contact with the reactive solution, although no transformation to crystalline phase occurs. Indeed, immediately after the addition of synthetic ACC into the reactive solutions, up to 3 wt.% of this solid dissolved until the solution reached saturation with respect to this phase (Fig. 6C). At the same time, the remaining amorphous solid became enriched in Mg and SO_4 (Table 1 and Fig. 9A) owing to a highly dynamic exchange of solutes between the solution and the solid phase (≤0.2 min), similar to that observed earlier by Purgstaller et al. (2019). Goodwin et al. (2010) have shown that ACC consists of a nanoporous framework that supports interconnected chan-

Table 2
Apparent precipitation rates (r_i) calculated based on the temporal evolution of the reactive solution during ACC transformation.

Experiment	SO_4 (mM)	r_i (mM/min)
s0	0	1.23
s10	10	1.12
s30	30	1.06
s30_2	30	1.07
s45	45	0.99
s75	75	0.79
s90	90	0.73

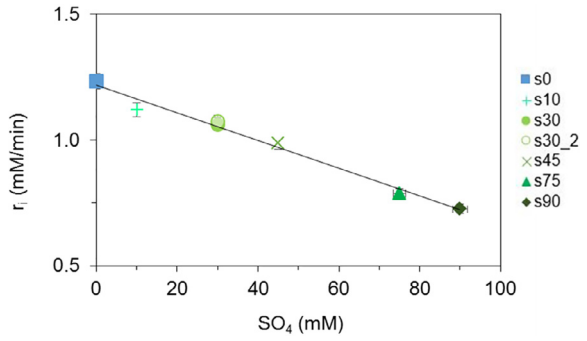

Fig. 7. Apparent precipitation rate (r_i) during stage II plotted as a function of initial sulfate concentration in the reactive solution.

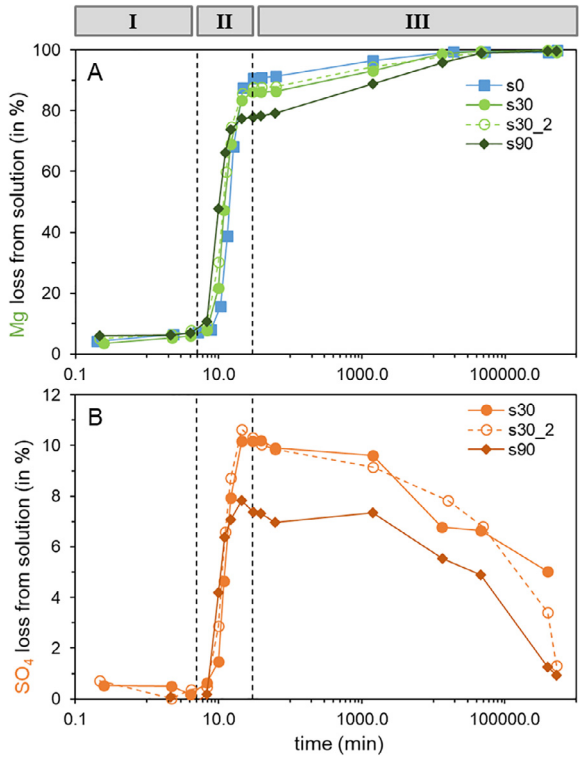

Fig. 8. Long-term chemical evolution up to 1 year of reaction time A) Mg concentration, B) SO_4 concentration.

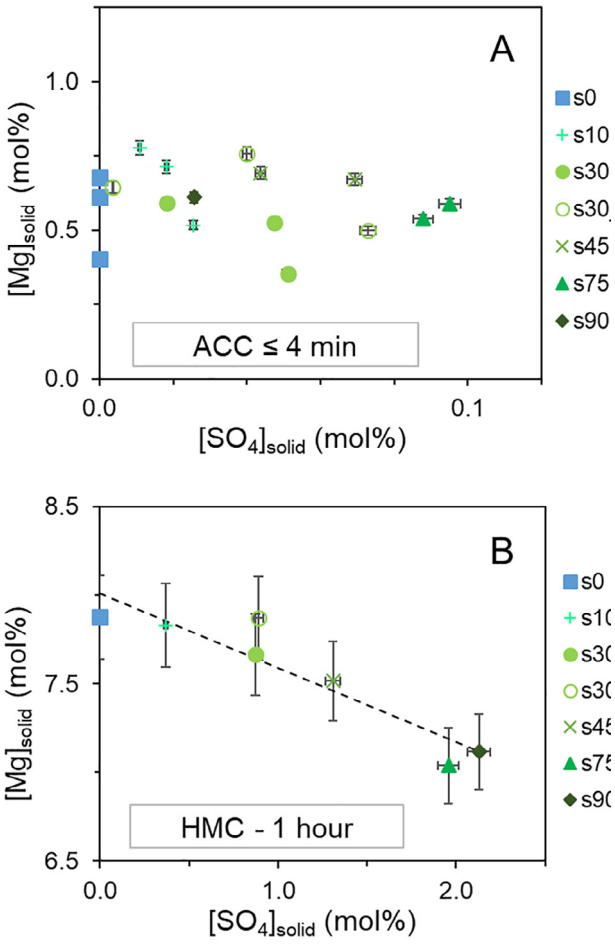

Fig. 9. Chemical composition of the solids during stage I and III. A) Mg and SO_4 contents of ACC within 4 min of reaction time show no correlation. B) Mg and SO_4 contents of HMC collected after 1 h of reaction time show an anticorrelation.

nels containing water and carbonate molecules. This nanoporous structure of ACC provides large surface areas (Sun et al., 2018, 2019) for fast exchange of solutes between the ACC and the reactive solution. Likely the presence of this network explains the enrichment of the bulk amorphous solid in Mg and SO_4 (Table 1).

The observed enrichment of ACC in Mg and SO_4 however, is not simply due to the presence of these ions in the pore fluid, but actual substitution in the structure of the solid. Evidence to this is provided from the infrared spectra of ACC which was sampled from the experiments performed in the presence of SO_4^{2-}(aq). The incorporation of SO_4 in the solid phase reveals a broad band at 1134/1160 cm^{-1} besides the characteristic vibration bands of CO_3 (Fig. 4). This band can be assigned to internal ν_3 vibrations of SO_4, similar to that observed in SO_4-bearing synthetic calcite (Takano et al., 1980). The distinct difference of the position of this band to that of the ν_3 vibrational band of SO_4^{2-}(aq) species at 1100 cm^{-1} (Hug, 1997; Wei et al., 2005), suggests that SO_4 in ACC cannot be assigned to SO_4^{2-}(aq) within the nanoporous network of ACC, but is rather incorporated in the bonding environment of the solid

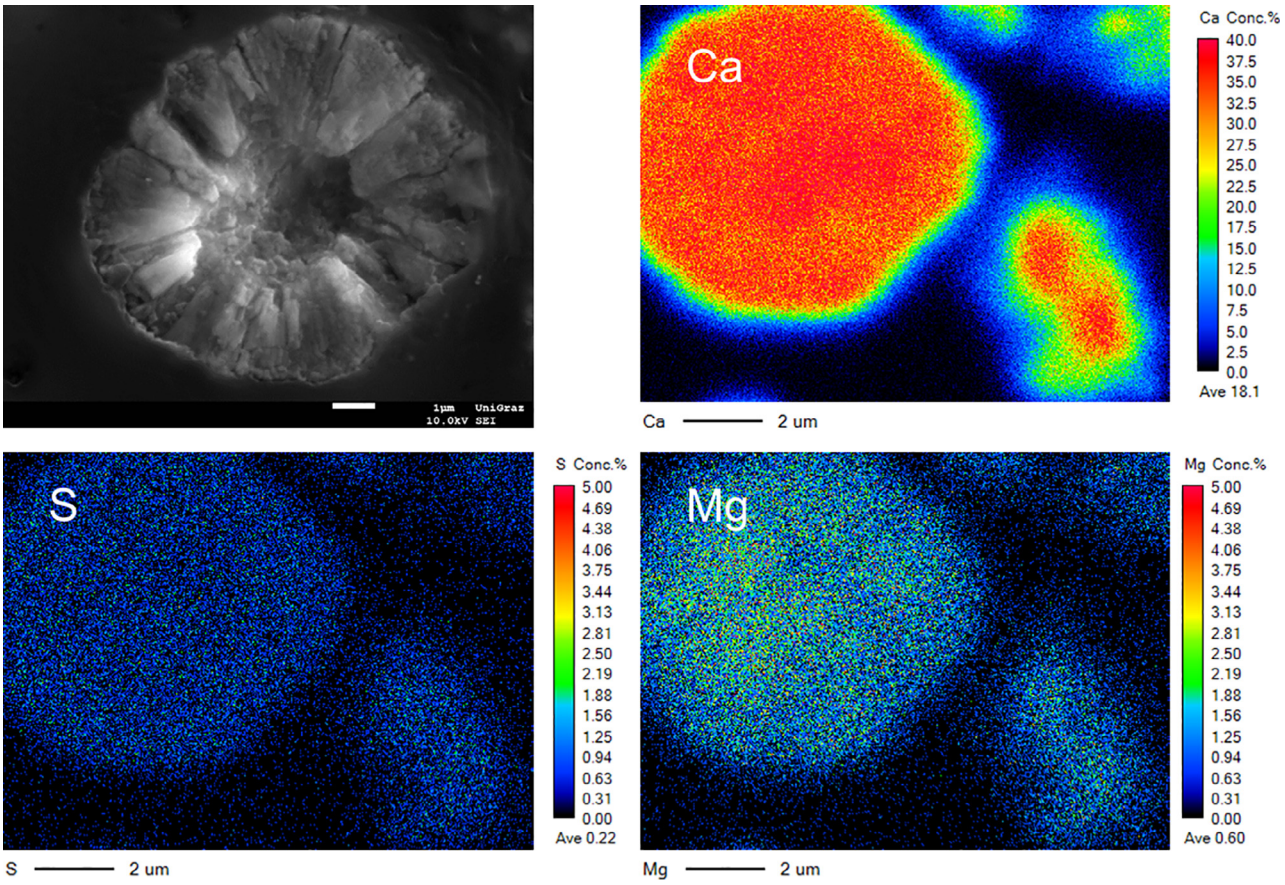

Fig. 10. Element distribution images of HMC collected after 1 day of reaction time (s90_12).

phase. The same can be suggested for the presence of Mg in ACC structure. Indeed in agreement with the earlier observations by Huang et al. (2018) a shift of ν_1 from 1074 cm^{-1} towards higher frequencies at 1075 cm^{-1} was recorded in the collected FTIR spectra. This distinctive but small shift denotes a distortion of the short-range order of ACC. Note here, vibration bands of other Mg-bearing phases (e.g. brucite, hydromagnesite) were not detected by *in situ* Raman or FTIR at any time during the experimental runs hence the Mg loss in the reactive solution can only be assigned to the transfer of Mg from the solution to the amorphous phase.

4.2. Controls of aqueous complexation on ACC transformation to HMC

An interesting finding of this study is that the synthetic ACC, added into the HCO_3-Mg-(SO_4-)bearing solutions, exhibits a prolonged metastability of up to 12 minutes (experiment s0) before it transforms into HMC (Fig. 3). This behavior comes in contrast to earlier observations suggesting instant ACC transformation ($\leq$30 s) into crystalline calcium carbonate polymorphs (e.g. vaterite and calcite) in an additive-free aqueous solution (Bots et al., 2012; Rodriguez-Blanco et al., 2012). Similarly, the stability of ACC in this study cannot be assigned to the presence of Mg in the amorphous solid as it was suggested earlier by Lin et al. (2015). In their study, the structural water bound to Mg ions was suggested to increase considerably the activation energy associated with the dehydration of ACC; a process that has been described to occur before crystallization (Ihli et al., 2014) and is based on the fact that Mg dehydration rate (10^5 s^{-1}) is 4 orders of magnitude slower compared to Ca (10^9 s^{-1}) (Lincoln and Merbach, 1995; Bleuzen et al., 1997).

Within the experimental runs of this study, the initially Mg-free ACC, is becoming enriched in Mg within the first 4 min of reaction time, however, it exhibits the same content of 0.6 $\pm$ 0.2 mol% Mg (Fig. 9A) in all the experimental runs. Yet as it can be seen in Fig. 3A, the onset of transformation of ACC to crystalline material is varying among the experimental runs and is associated with the concentration of $MgSO_4^0$ in the reactive solution. Note here, that during the transformation when ACC dissolves and HMC is forming, all solutions are undersaturated with respect to calcium sulfate phases such as gypsum and bassanite (Table S1) and the presence of calcium sulfate phases was not confirmed by Raman, FTIR, XRD or SEM. The obtained results suggest that ACC transformation to HMC is controlled by the abundance of Mg^{2+}(aq), which is a function of SO_4 concentration in experimental runs of this study. Indeed, in the present study, the initial total Mg concentration was the same in all the experiments (~27 mM; Table 1), but the presence of SO_4 strongly

reduced the concentration of free Mg ions, Mg^{2+} (aq), due to the formation of the $MgSO_4^0$ aquo complex (Table S1). In the experiment with the highest SO_4 concentration (i.e. s90; 90 mM) Mg^{2+}(aq) represents only 44% of the total Mg concentration, whereas in the SO_4-free experiment (s0) Mg^{2+}(-aq) accounts for 73% of the total Mg concentration. Indeed, the obtained linear correlation between the concentration of Mg^{2+} (aq) and the onset of HMC formation (Fig. 3B) indicates that the delay of ACC transformation is strongly controlled by the retarding effect of aqueous Mg^{2+} on calcite nucleation (Fernández-Díaz et al., 1996; Du and Amstad, 2020). In contrast, SO_4^{2-}(aq) is not retarding the nucleation of calcite, as it is indicated by the reverse trend between SO_4 concentration and the onset of HMC formation (Fig. 3A). Thus, the formation of $MgSO_4^0$ aquo complexes, is the factor controlling the abundance of Mg^{2+}(aq) and subsequently the nucleation of HMC (Fig. 3B).

The obtained results allow the quantification of the effect of dissolved SO_4 on the transformation of ACC to HMC, using the apparent HMC precipitation rate (r_i). As it is illustrated in Fig. 6, r_i decreases with increasing SO_4 concentrations in the reactive solutions (Table 2). Considering that crystalline HMC growth proceeds via ion-by-ion addition of dissolved chemical species to advancing steps at the crystal surface (Burton et al., 1951), complexation of SO_4 with aqueous Ca^{2+} and Mg^{2+} is effectively reducing their abundance in the reactive solution (see Table S1) which results in a decreased apparent precipitation rate (Fig. 7). Similar, Han et al. (2017) observed decreased precipitation rates of Mg calcite and aragonite in the presence of $MgSO_4$ and comparable behavior has been seen from results by Nielsen et al. (2016) using a constant composition experimental approach to monitor the individual and combined effects of Mg^{2+} and SO_4^{2-}. Moreover, higher SO_4 concentrations caused lower Mg^{2+}/Ca^{2+} ratios at the time of transformation and resulted in reduced Mg uptake of HMC during transformation (Fig. 9B), an observation that comes in agreement with that of Purgstaller et al. (2021) who found that the prevailing Mg^{2+}/Ca^{2+} ratio of the reactive solution at the time of transformation is the main controlling parameter for enhanced Mg incorporation in HMC.

Previous ACC transformation experiments have shown that the mineralogy of the crystalline product is controlled by the prevailing physicochemical parameters of the experimental solution including pH, temperature and Mg^{2+}/Ca^{2+} ratio (Blue et al., 2017; Purgstaller et al., 2017a,b; Konrad et al., 2018). In the present study, a prevailing Mg^{2+}/Ca^{2+} ratio between 4 and 5 yielded into the formation of HMC, which is in good agreement with results obtained by Blue et al. (2017) and Purgstaller et al. (2017a). Variations in SO_4 concentrations (10–90 mM) had no effect on the pathway of ACC transformation and HMC has been the only resulting crystalline phase. This behaviour comes in contrast to mineral growth experiments where inhibitory effects on low-Mg calcite growth have been observed in the presence of SO_4 ions, promoting aragonite formation instead of calcite (Goetschl et al., 2019), an observation that has important consequences for the interpretation of temporal variations of the primary $CaCO_3$ polymorph in marine environments (Bots et al., 2011). However, the SO_4/CO_3 ratios of the experimental solutions in which an inhibiting effect on calcite formation was observed have been considerably higher compared to the current experimental conditions.

4.3. HMC formed via ACC and implications for natural carbonates

The most interesting feature of this study is that the Mg content of the nanocrystalline HMC is increasing during the whole duration of stage III that lasted until the end of the experimental runs after 1 year of reaction time. The fast precipitation of HMC (10^{-5} mol s^{-1}) resulted in the formation of aggregates with nanometer sized crystal subunits and a radial-columnar internal structure. The HMC that was initially formed after the transformation of ACC was likely highly porous (Fig. 5B) and its Mg content was affected by both precipitation kinetics (e.g. Mavromatis et al., 2013; Goetschl et al., 2019) and prevailing Mg^{2+}/Ca^{2+} ratio (e.g. Mucci and Morse, 1983; Blue et al. 2017; Purgstaller et al., 2021). In the experimental runs of this study both growth kinetics and Mg^{2+}/Ca^{2+} ratio are affected by the aqueous SO_4 concentration (Fig. 7 and Table S1).

After the complete transformation of ACC into HMC, however, the crystalline solids exhibit changes in their Mg and SO_4 content as a function of time in a process that occurs during the whole duration of the experimental runs up to 1 year of reaction time as it can be seen in Fig. 8. These changes in chemical composition suggest a continuous exchange reaction between solid and solution following a process that is likely controlled by the high reactive surface of the solid as it is evidenced by the high porosity of the nanocrystalline material (Fig. 5B and Fig. S5). Indeed, the measured specific surface area of ACC and nanocrystalline calcite are typically high between 14 and 42 m^2/g (Schultz et al., 2013; Radha and Navrotsky, 2015; Konrad et al., 2016). Interestingly, the continuous enrichment of the solid in Mg during stage III is accompanied by a decrease of its SO_4 content (Table 1; Fig. 8). The Mg-SO_4-anticorrelation of calcite samples observed in this study becomes more pronounced when the reactive solutions achieve chemical compositions that reflect near thermodynamic equilibrium conditions (Table S1). This process is likely related to the contrasting effect caused by the presence of Mg and SO_4 in the crystall lattice of calcite. Indeed, the incorporation of Mg into calcite is causing unit cell contraction (Paquette and Reeder, 1990), whereas the uptake of SO_4 into calcite results in unit cell expansion (Kontrec et al., 2004). As such the enrichment of both ions in nanocrystalline calcite derived from ACC is rather unlikely to occur, a feature which has also been observed during seeded growth of low-Mg calcite (Goetschl et al., 2019).

The continuous exchange of Mg and SO_4 between the solid and the reactive solution is affecting the total mass of the nanocrystalline aggregates with a homogeneous distribution of Mg and SO_4 and is not limited only to the outer rim of the aggregates. This is evident from the comparison

of the elemental distribution maps of calcite collected after 1 day (Fig. 10; Table S2) and after 1 year (Fig. S7; Table S2) in the experiment s90. This observation has major implications for the interpretation of chemical signals in natural carbonates that form via an amorphous precursor, especially if they remain in contact with an aqueous fluid after their initial formation and subsequent transformation. For example, Littlewood et al. (2017) have shown elevated concentrations of Sr in calcite formed from an amorphous precursor. Similar to the behavior of SO_4 in our study it is likely that the high Sr content in ACC derived calcite is not retained after longer period of contact with an aqueous phase. Earlier studies have shown that up to 10 unit cells below crystal surface can participate in elemental and isotope exchange between a carbonate mineral phase and the reactive solution (Stipp et al., 1998; Mavromatis et al., 2016, 2017c). In contrast the homogeneous distribution of Mg in calcite that was observed in this study (Fig. 10 and Fig. S7; Table S2) suggest that the chemical composition of the solid would not be preserved, if the composition of the fluid phase is significantly altered. Similar observations have been made for HMC formed from an amorphous precursor using Mg and O isotopes (Mavromatis et al., 2017b; Dietzel et al., 2020). These earlier studies suggest that rapidly after transformation from ACC to calcite isotopic equilibrium is achieved and no information of the isotopic signals of the amorphous precursor is recorded. Considering that ACC precursors commonly occur during the formation of biominerals (Addadi et al., 2003; Du and Amstad, 2020) but also in inorganic environments such as speleothems (Demény et al., 2016), the obtained results suggest that caution is needed for the interpretation of their chemical and likely isotopic signals as environmental proxies.

Additionally the results of this study suggest that nanostructured HMCs with high internal porosity that frequently form in natural environments have a considerable potential for secondary changes of their geochemical signature due to occurring mineral-fluid interactions. Carbonates are subject to variable degrees of post-depositional/post-mortem alteration which may be easily intensified and accelerated if the mineral owns a large reaction surface for ion exchange (Pederson et al., 2020). Hence, determining and quantifying secondary exchange reactions during mineral-fluid interactions of nanocrystalline HMC is urgently required to define the robustness of geochemical proxies obtained from these solids. On a different view, these nanocrystalline HMCs may indicate distinct reaction pathways and/or environmental conditions of the storage and transformation media.

5. CONCLUSIONS

In this study we examined the transformation of synthetic ACC in reactive solution containing ~27 mM Mg and variable SO_4 concentrations up to 90 mM. In these experiments, the solid remained in contact with the reactive solution - after the transformation of ACC into HMC - for 1 year and it was characterized for its chemical and mineralogical composition. The obtained results suggest that aqueous complexation of Mg^{2+} with SO_4^{2-} and the formation of $MgSO_4^0$(aq) is the factor controlling the stability of ACC in the reactive solution. Indeed calcite nucleation is a function of free Mg^{2+} ion concentration in the reactive solution and the formation of $MgSO_4^0$ aquo complexes reduces its availability and subsequently allows for earlier transformation of the amorphous phase to calcite. The nanocrystalline HMC formed from ACC exhibits a homogeneous distribution of Mg and SO_4 as it was revealed by electron microprobe. Interestingly, HMC remained nanocrystalline after 1 year in contact with the reactive solution, but became progressingly enriched in Mg and depleted in SO_4. These changes in chemical composition affecting the total mass of the HMC aggregates suggest a continuous exchange process between solid and solution as long as they are in contact. The findings of this study suggest that calcite formed via an amorphous precursor may still be highly reactive in exchanging compounds and as such the chemical and isotopic signals recorded at the time of mineral formation can be reset by interacting with natural fluids of different chemical and/or isotopic composition during and after deposition.

Declaration of Competing Interest

The authors declare that they have no known competing financial interests or personal relationships that could have appeared to influence the work reported in this paper.

ACKNOWLEDGEMENTS

The authors are thankful to Judith Jernej for her assistance with IC analyses. Our colleagues Jean-Michel Brazier and Florian Steindl are highly acknowledged for fruitful discussions during the preparation of this manuscript. Chemical and mineralogical analyses were conducted at NAWI Graz Central Lab for Water, Minerals and Rocks. This work has been funded through DFG-FWF collarborative research initiative CHARON II (DFG Forschergruppe 1644; FWF I3028-N29) and supported by FWF project T920-N29 and NAWI Graz. The authors greatly appreciate the handling of the manuscript by Mariette Wolthers and the constructive comments of three anonymous reviewers.

APPENDIX A. SUPPLEMENTARY MATERIAL

Supplementary data to this article can be found online at https://doi.org/10.1016/j.gca.2021.07.026.

REFERENCES

Addadi L., Raz S. and Weiner S. (2003) Taking advantage of disorder: Amorphous calcium carbonate and its roles in biomineralization. *Adv. Mater.* **15**, 959–970.

Aizenberg J., Lambert G., Weiner S. and Addadi L. (2002) Factors involved in the formation of amorphous and crystalline calcium carbonate: A study of an ascidian skeleton. *J. Am. Chem. Soc.* **124**, 32–39.

Albéric M., Bertinetti L., Zou Z., Fratzl P., Habraken W. and Politi Y. (2018) The Crystallization of Amorphous Calcium

Carbonate is Kinetically Governed by Ion Impurities and Water. *Adv. Sci.*, 5.

Andersen F. A. and Brečević L. (1991) Infrared spectra of amorphous and crystalline calcium carbonate. *Acta Chem. Scand.* **45**, 1018–1024.

Balan E., Aufort J., Pouillé S., Dabos M., Blanchard M., Lazzeri M., Rollion-Bard C. and Blamart D. (2017) Infrared spectroscopic study of sulfate-bearing calcite from deep-sea bamboo coral. *Eur. J. Mineral.* **29**, 397–408.

Bischoff W. D., Sharma S. K. and MacKenzie F. T. (1985) Carbonate ion disorder in synthetic and biogenic magnesian calcites: a Raman spectral study. *Am. Mineral.* **70**, 581–589.

Bleuzen A., Pittet P. A., Helm L. and Merbach A. E. (1997) Water exchange on magnesium(II) in aqueous solution: A variable temperature and pressure ^{17}O NMR study. *Magn. Reson. Chem.* **35**, 765–773.

Blue C. R., Giuffre A., Mergelsberg S., Han N., De Yoreo J. J. and Dove P. M. (2017) Chemical and physical controls on the transformation of amorphous calcium carbonate into crystalline $CaCO_3$ polymorphs. *Geochim. Cosmochim. Acta* **196**, 179–196.

Bots P., Benning L. G., Rickaby R. E. M. and Shaw S. (2011) The role of SO_4 in the switch from calcite to aragonite seas. *Geology* **39**, 331–334.

Bots P., Benning L. G., Rodriguez-Blanco J.-D., Roncal-Herrero T. and Shaw S. (2012) Mechanistic Insights into the Crystallization of Amorphous Calcium Carbonate (ACC). *Cryst. Growth Des.* **12**, 3806–3814.

Böttcher M. E., Gehlken P. L. and Steele D. F. (1997) Characterization of inorganic and biogenic magnesian calcites by fourier transform infrared spectroscopy. *Solid State Ionics* **101–103**, 1379–1385.

Brečević L. and Nielsen A. E. (1989) Solubility of amorphous calcium carbonate. *J. Cryst. Growth* **98**, 504–510.

Burton E. A. and Walter L. M. (1991) The effects of P_{CO2} and temperature on magnesium incorporation in calcite in seawater and $MgCl_2$-$CaCl_2$ solutions. *Geochim. Cosmochim. Acta* **55**, 777–785.

Burton W. K., Cabrera N. and Frank F. C. (1951) The Growth of Crystals and the Equilibrium Structure of their Surfaces. *Phil. Trans. R. Soc. Lond.* **243**, 299–358.

Davis A. R. and Oliver B. G. (1972) A vibrational-spectroscopic study of the species present in the CO_2-H_2O system. *J. Solution Chem.* **1**, 329–339.

Demény A., Németh P., Czuppon G., Leél-Őssy S., Szabó M., Judik K., Németh T. and Stieber J. (2016) Formation of amorphous calcium carbonate in caves and its implications for speleothem research. *Sci. Rep.* **6**, 39602.

Dietzel M. (2011) Carbonates. *Encycl. Geobiol.*, 261–266.

Dietzel M., Purgstaller B., Kluge T., Leis A. and Mavromatis V. (2020) Oxygen and clumped isotope fractionation during the formation of Mg calcite via an amorphous precursor. *Geochim. Cosmochim. Acta* **276**, 258–273.

Du H. and Amstad E. (2020) Water: How Does It Influence the $CaCO_3$ Formation? *Angew. Chem. Int. Ed.* **59**, 1798–1816.

Du H., Steinacher M., Borca C., Huthwelker T., Murello A., Stellacci F. and Amstad E. (2018) Amorphous $CaCO_3$: Influence of the Formation Time on Its Degree of Hydration and Stability. *J. Am. Chem. Soc.* **140**, 14289–14299.

Evans D., Gray W. R., Rae J. W. B., Greenop R., Webb P. B., Penkman K., Kröger R. and Allison N. (2020) Trace and major element incorporation into amorphous calcium carbonate (ACC) precipitated from seawater. *Geochim. Cosmochim. Acta* **290**, 293–311.

Fernández-Díaz L., Putnis A., Prieto M. and Putnis C. V. (1996) The role of magnesium in the crystallization of calcite and aragonite in a porous medium. *J. Sediment. Res.* **66**, 482–491.

Floquet N., Vielzeuf D., Ferry D., Ricolleau A., Heresanu V., Perrin J., Laporte D. and Fitch A. N. (2015) Thermally Induced Modifications and Phase Transformations of Red Coral Mg-Calcite Skeletons from Infrared Spectroscopy and High Resolution Synchrotron Powder Diffraction Analyses. *Cryst. Growth Des.* **15**, 3690–3706.

Fujita K. and Kimura M. (1981) The Raman Band Shape and Vibrational Relaxation of the v_1 Mode of SO_4^{2-} in Na_2SO_4 and $(NH_4)_2SO_4$ Aqueous Solutions. *J. Raman Spectrosc.* **11**, 108–111.

Gautier Q., Bénézeth P., Mavromatis V. and Schott J. (2014) Hydromagnesite solubility product and growth kinetics in aqueous solution from 25 to 75°C. *Geochim. Cosmochim. Acta* **138**, 1–20.

Gebauer D. and Cölfen H. (2011) Prenucleation clusters and non-classical nucleation. *Nano Today* **6**, 564–584.

Gebauer D., Gunawidjaja P. N., Ko J. Y. P., Bacsik Z., Aziz B., Liu L., Hu Y., Bergström L., Tai C. W., Sham T. K., Edén M. and Hedin N. (2010) Proto-calcite and proto-vaterite in amorphous calcium carbonates. *Angew. Chem. Int. Ed.* **49**, 8889–8891.

Giuffre A. J., Gagnon A. C., De Yoreo J. J. and Dove P. M. (2015) Isotopic tracer evidence for the amorphous calcium carbonate to calcite transformation by dissolution–reprecipitation. *Geochim. Cosmochim. Acta* **165**, 407–417.

Goetschl K. E., Purgstaller B., Dietzel M. and Mavromatis V. (2019) Effect of sulfate on magnesium incorporation in low-magnesium calcite. *Geochim. Cosmochim. Acta* **265**, 505–519.

Goldsmith J. R., Graf D. L. and Heard H. C. (1961) Lattice constants of the calcium-magnesium carbonates. *Am. Mineral.* **46**, 453–459.

Gong Y., Killian C., Olson I., Appathurai N. P., Amasino A., Martin M., Holt L., Wilt F. and Gilbert P. (2012) Phase transitions in biogenic amorphous calcium carbonate. *Proc. Natl. Acad. Sci. USA* **109**, 6088–6093.

Goodwin A. L., Michel F. M., Phillips B. L., Keen D. A., Dove M. T. and Reeder R. J. (2010) Nanoporous structure and medium-range order in synthetic amorphous calcium carbonate. *Chem. Mater.* **22**, 3197–3205.

Gower L. B. (2008) Biomimetic model systems for investigating the amorphous precursor pathway and its role in biomineralization. *Chem. Rev.* **108**, 4551–4627.

Han M., Zhao Y., Zhao H., Han Z., Yan H., Sun B., Meng R., Zhuang D., Li D. and Liu B. (2017) A comparison of amorphous calcium carbonate crystallization in aqueous solutions of $MgCl_2$ and $MgSO_4$: implications for paleo-ocean chemistry. *Mineral. Petrol.*, 1–16.

Harrison A. L., Mavromatis V., Oelkers E. H. and Bénézeth P. (2019) Solubility of the hydrated Mg-carbonates nesquehonite and dypingite from 5 to 35 °C: Implications for CO_2 storage and the relative stability of Mg-carbonates. *Chem. Geol.* **504**, 123–135.

Huang Y. C., Gindele M. B., Knaus J., Rao A. and Gebauer D. (2018) On mechanisms of mesocrystal formation: Magnesium ions and water environments regulate the crystallization of amorphous minerals. *CrystEngComm* **20**, 4395–4405.

Hug S. J. (1997) In situ fourier transform infrared measurements of sulfate adsorption on hematite in aqueous solutions. *J. Colloid Interface Sci.* **188**, 415–422.

Ihli J., Kim Y. Y., Noel E. H. and Meldrum F. C. (2013) The effect of additives on amorphous calcium carbonate (ACC): Janus behavior in solution and the solid state. *Adv. Funct. Mater.* **23**, 1575–1585.

Ihli J., Wong W. C., Noel E. H., Kim Y. Y., Kulak A. N., Christenson H. K., Duer M. J. and Meldrum F. C. (2014)

Dehydration and crystallization of amorphous calcium carbonate in solution and in air. *Nat. Commun.* **5**, 1–10.

Jiang J., Gao M. R., Qiu Y. H., Wang G. S., Liu L., Cai G. Bi, Bin and Yu S. H. (2011) Confined crystallization of polycrystalline high-magnesium calcite from compact Mg-ACC precursor tablets and its biological implications. *CrystEngComm* **13**, 952–956.

Jin W., Jiang S., Pan H. and Tang R. (2018) Amorphous phase mediated crystallization: Fundamentals of biomineralization. *Crystals* **8**, 23–26.

Konrad F., Gallien F., Gerard D. E. and Dietzel M. (2016) Transformation of Amorphous Calcium Carbonate in Air. *Cryst. Growth Des.* **16**, 6310–6317.

Konrad F., Purgstaller B., Gallien F., Mavromatis V., Gane P. and Dietzel M. (2018) Influence of aqueous Mg concentration on the transformation of amorphous calcium carbonate. *J. Cryst. Growth* **498**, 381–390.

Kontrec J., Kralj D., Brečević L., Falini G., Fermani S., Noethig-Laslo V. and Mirosavljević K. (2004) Incorporation of inorganic anions in calcite. *Eur. J. Inorg. Chem.*, 4579–4585.

Lin C.-J., Yang S.-Y., Huang S.-J. and Chan J. C. C. (2015) Structural Characterization of Mg-Stabilized Amorphous Calcium Carbonate by Mg-25 Solid-State NMR Spectroscopy. *J. Phys. Chem. C* **119**, 7225–7233.

Lincoln S. F. and Merbach A. E. (1995) Substitution reactions of solvated metal ions. *Adv. Inorg. Chem.* **42**, 1–88.

Littlewood J. L., Shaw S., Peacock C. L., Bots P., Trivedi D. and Burke I. T. (2017) Mechanism of Enhanced Strontium Uptake into Calcite via an Amorphous Calcium Carbonate Crystallization Pathway. *Cryst. Growth Des.* **17**, 1214–1223.

Long X., Ma Y. and Qi L. (2014) Biogenic and synthetic high magnesium calcite - A review. *J. Struct. Biol.* **185**, 1–14.

Long X., Ma Y. and Qi L. (2011) In vitro synthesis of high Mg calcite under ambient conditions and its implication for biomineralization process. *Cryst. Growth Des.* **11**, 2866–2873.

Lorens R. B. (1981) Sr, Cd, Mn and Co distribution coefficients in calcite as a function of calcite precipitation rate. *Geochim. Cosmochim. Acta* **45**, 553–561.

Loste E., Wilson R. M., Seshadri R. and Meldrum F. C. (2003) The role of magnesium in stabilising amorphous calcium carbonate and controlling calcite morphologies. *J. Cryst. Growth* **254**, 206–218.

Mavromatis V., Gautier Q., Bosc O. and Schott J. (2013) Kinetics of Mg partition and Mg stable isotope fractionation during its incorporation in calcite. *Geochim. Cosmochim. Acta* **114**, 188–203.

Mavromatis V., Goetschl K. E., Grengg C., Konrad F., Purgstaller B. and Dietzel M. (2018) Barium partitioning in calcite and aragonite as a function of growth rate. *Geochim. Cosmochim. Acta* **237**, 65–78.

Mavromatis V., Harrison A. L., Eisenhauer A. and Dietzel M. (2017c) Strontium isotope fractionation during strontianite ($SrCO_3$) dissolution, precipitation and at equilibrium. *Geochim. Cosmochim. Acta* **218**, 201–204.

Mavromatis V., Immenhauser A., Buhl D., Purgstaller B., Baldermann A. and Dietzel M. (2017a) Effect of organic ligands on Mg partitioning and Mg isotope fractionation during low-temperature precipitation of calcite in the absence of growth rate effects. *Geochim. Cosmochim. Acta* **207**, 139–153.

Mavromatis V., Montouillout V., Noireaux J., Gaillardet J. and Schott J. (2015) Characterization of boron incorporation and speciation in calcite and aragonite from co-precipitation experiments under controlled pH, temperature and precipitation rate. *Geochim. Cosmochim. Acta* **150**, 299–313.

Mavromatis V., Purgstaller B., Dietzel M., Buhl D., Immenhauser A. and Schott J. (2017b) Impact of amorphous precursor phases on magnesium isotope signatures of Mg-calcite. *Earth Planet. Sci. Lett.* **464**, 227–236.

Mavromatis V., Schmidt M., Botz R., Comas-Bru L. and Oelkers E. H. (2012) Experimental quantification of the effect of Mg on calcite-aqueous fluid oxygen isotope fractionation. *Chem. Geol.* **310–311**, 97–105.

Mavromatis V., van Zuilen K., Purgstaller B., Baldermann A., Nägler T. F. and Dietzel M. (2016) Barium isotope fractionation during witherite ($BaCO_3$) dissolution, precipitation and at equilibrium. *Geochim. Cosmochim. Acta* **190**, 72–84.

Mergelsberg S. T., De Yoreo J. J., Miller Q. R. S., Marc Michel F., Ulrich R. N. and Dove P. M. (2020) Metastable solubility and local structure of amorphous calcium carbonate (ACC). *Geochim. Cosmochim. Acta* **289**, 196–206.

Milliman J. D., Gastner M. and Müller J. (1971) Utilization of Magnesium in Coralline Algae Utilization of Magnesium in Coralline Algae. *Geol. Soc. Am. Bull.* **82**, 573–580.

Morse J. W. and Mackenzie F. T. (1990) *Geochemistry of sedimentary carbonates*. Elsevier, Amsterdam, Oxford, New York, Tokyo.

Mucci A. and Morse J. W. (1983) The incorporation of Mg^{2+} and Sr^{2+} into calcite overgrowths: influences of growth rate and solution composition. *Geochim. Cosmochim. Acta* **47**, 217–233.

Nielsen M. R., Sand K. K., Rodriguez-Blanco J. D., Bovet N., Generosi J., Dalby K. N. and Stipp S. L. S. (2016) Inhibition of Calcite Growth: Combined Effects of Mg^{2+} and SO_4^{2-}. *Cryst. Growth Des.* **16**, 6199–6207.

Oelkers E. H., Pogge von Strandmann P. A. E. and Mavromatis V. (2019) The rapid resetting of the Ca isotopic signatures of calcite at ambient temperature during its congruent dissolution, precipitation, and at equilibrium. *Chem. Geol.* **512**, 1–10.

Paquette J. and Reeder R. J. (1990) Single-crystal X-ray structure refinements of two biogenic magnesian calcite crystals. *Am. Mineral.* **75**, 1151–1158.

Pederson C. L., Mavromatis V., Dietzel M., Rollion-Bard C., Breitenbach S. F. M., Yu D., Nehrke G. and Immenhauser A. (2020) Variation in the diagenetic response of aragonite archives to hydrothermal alteration. *Sed. Geol.* **406** 105716.

Politi Y., Batchelor D. R., Zaslansky P., Chmelka B. F., Weaver J. C., Sagi I., Weiner S. and Addadi L. (2010) Role of magnesium ion in the stabilization of biogenic amorphous calcium carbonate: A structure-function investigation. *Chem. Mater.* **22**, 161–166.

Purgstaller B., Dietzel M., Baldermann A. and Mavromatis V. (2017b) Control of temperature and aqueous Mg^{2+}/Ca^{2+} ratio on the (trans-)formation of ikaite. *Geochim. Cosmochim. Acta* **217**, 128–143.

Purgstaller B., Goetschl K. E., Mavromatis V. and Dietzel M. (2019) Solubility investigations in the amorphous calcium magnesium carbonate system. *CrystEngComm* **21**, 155–164.

Purgstaller B., Konrad F., Dietzel M., Immenhauser A. and Mavromatis V. (2017a) Control of Mg^{2+}/Ca^{2+} Activity Ratio on the Formation of Crystalline Carbonate Minerals via an Amorphous Precursor. *Cryst. Growth Des.* **17**, 1069–1078.

Purgstaller B., Mavromatis V., Goetschl K. E., Steindl F. R. and Dietzel M. (2021) Effect of temperature on the transformation of amorphous calcium magnesium carbonate with near-dolomite stoichiometry into high Mg-calcite. *CrystEngComm* **23**, 1969–1981.

Purgstaller B., Mavromatis V., Immenhauser A. and Dietzel M. (2016) Transformation of Mg-bearing amorphous calcium carbonate to Mg-calcite - In situ monitoring. *Geochim. Cosmochim. Acta* **174**, 180–195.

Radha A. V. and Navrotsky A. (2015) Direct experimental measurement of water interaction energetics in amorphous

carbonates MCO_3 (M = Ca, Mn, and Mg) and implications for carbonate crystal growth. *Cryst. Growth Des.* **15**, 70–78.

Raz S., Weiner S. and Addadi L. (2000) Formation of high-magnesian calcites via an amorphous precursor phase: Possible biological implications. *Adv. Mater.* **12**, 38–42.

Reeder R. J. (1990) Carbonates: Mineralogy and Chemistry. *Rev. Mineral Geochem.*, 11.

Rodriguez-Blanco J. D., Shaw S., Bots P., Roncal-Herrero T. and Benning L. G. (2012) The role of pH and Mg on the stability and crystallization of amorphous calcium carbonate. *J. Alloy. Compd.*, S477–S479.

Rodriguez-Navarro C., Kudłacz K., Cizer Ö. and Ruiz-Agudo E. (2015) Formation of amorphous calcium carbonate and its transformation into mesostructured calcite. *CrystEngComm* **17**, 58–72.

Schmidt M. P., Ilott A. J., Phillips B. L. and Reeder R. J. (2014) Structural changes upon dehydration of amorphous calcium carbonate. *Cryst. Growth Des.* **14**, 938–951.

Schultz L. N., Andersson M. P., Dalby K. N., Müter D., Okhrimenko D. V., Fordsmand H. and Stipp S. L. S. (2013) High surface area calcite. *J. Cryst. Growth* **371**, 34–38.

Shen L., Sippola H., Li X., Lindberg D. and Taskinen P. (2019) Thermodynamic Modeling of Calcium Sulfate Hydrates in the $CaSO_4$-H_2O System from 273.15 to 473.15 K with Extension to 548.15 K. *J. Chem. Eng. Data* **64**, 2697–2709.

Stipp S. L. S., Konnerup-Madsen J., Franzreb K., Kulik A. and Mathieu H. J. (1998) Spontaneous movement of ions through calcite at standard temperature and pressure. *Nature* **396**, 356–359.

Sun R., Willhammar T., Svensson Grape E., Strømme M. and Cheung O. (2019) Mesoscale Transformation of Amorphous Calcium Carbonate to Porous Vaterite Microparticles with Morphology Control. *Cryst. Growth Des.* **19**, 5075–5087.

Sun R., Zhang P., Bajnóczi É. G., Neagu A., Tai C. W., Persson I., Strømme M. and Cheung O. (2018) Amorphous Calcium Carbonate Constructed from Nanoparticle Aggregates with Unprecedented Surface Area and Mesoporosity. *ACS Appl. Mater. Interfaces* **10**, 21556–21564.

Sun S., Chevrier D. M., Zhang P., Gebauer D. and Cölfen H. (2016) Distinct Short-Range Order Is Inherent to Small Amorphous Calcium Carbonate Clusters (<2 nm). *Angew. Chem. Int. Ed.* **55**, 12206–12209.

Takano B., Asano Y. and Watanuki K. (1980) Characterization of sulfate ion in travertine. *Contrib. Mineral. Petrol.* **72**, 197–203.

Tobler D. J., Rodriguez Blanco J. D., Sørensen H. O., Stipp S. L. S. and Dideriksen K. (2016) Effect of pH on Amorphous Calcium Carbonate Structure and Transformation. *Cryst. Growth Des.* **16**, 4500–4508.

Uchikawa J., Harper D. T., Penman D. E., Zachos J. C. and Zeebe R. E. (2017) Influence of solution chemistry on the boron content in inorganic calcite grown in artificial seawater. *Geochim. Cosmochim. Acta* **218**, 291–307.

Wang D., Hamm L. M., Bodnar R. J. and Dove P. M. (2012) Raman spectroscopic characterization of the magnesium content in amorphous calcium carbonates. *J. Raman Spectrosc.* **43**, 543–548.

Wang F., Zhang Y. H., Li S. H., Wang L. Y. and Zhao L. J. (2005) A strategy for single supersaturated droplet analysis: Confocal Raman investigations on the complicated hygroscopic properties of individual $MgSO_4$ droplets on the quartz substrate. *Anal. Chem.* **77**, 7148–7155.

Wei Z. F., Zhang Y. H., Zhao L. J., Liu J. H. and Li X. H. (2005) Observation of the first hydration layer of isolated cations and anions through the FTIR-ATR difference spectra. *J. Phys. Chem. A* **109**, 1337–1342.

White W. B. (1974) The carbonate minerals. In *The Infrared Spectra of Minerals*, pp. 227–284.

Xto J. M., Du H., Borca C. N., Amstad E., Van Bokhoven J. A. and Huthwelker T. (2019) Tuning the Incorporation of Magnesium into Calcite during Its Crystallization from Additive-Free Aqueous Solution. *Cryst. Growth Des.* **19**, 4385–4394.

De Yoreo J. J., Gilbert P. U. P. A., Sommerdijk N. A. J. M., Penn R. L., Whitelam S., Joester D., Zhang H., Rimer J. D., Navrotsky A., Banfield J. F., Wallace A. F., Michel F. M., Meldrum F. C., Colfen H. and Dove P. M. (2015) Crystallization by particle attachment in synthetic, biogenic, and geologic environments. *Science* **349**, aaa6760.

Zou Z., Polishchuk I., Bertinetti L., Pokroy B., Politi Y., Fratzl P. and Habraken W. J. E. M. (2018) Additives influence the phase behavior of calcium carbonate solution by a cooperative ion-association process. *J. Mater. Chem. B* **6**, 449–457.

Associate editor: Mariette Wolthers